

NASA  
TP  
1179  
c.1

# NASA Technical Paper 1179



## Static and Dynamic Stability Analysis of the Space Shuttle Vehicle-Orbiter

LOAN COPY: RETURN TO  
AFWL TECHNICAL LIBRA  
KIRTLAND AFB, N. M.

Wei J. Chyu, Ralph K. Cavin,  
and Larry L. Erickson

MARCH 1978

NASA



0134536

## NASA Technical Paper 1179

# Static and Dynamic Stability Analysis of the Space Shuttle Vehicle-Orbiter

Wei J. Chyu

*Ames Research Center, Moffett Field, California*

Ralph K. Cavin

*Texas A&M University, College Station, Texas*

Larry L. Erickson

*Ames Research Center, Moffett Field, California*



National Aeronautics  
and Space Administration

**Scientific and Technical  
Information Office**

1978

## TABLE OF CONTENTS

	Page
<b>SYMBOLS . . . . .</b>	<b>iii</b>
<b>SUMMARY . . . . .</b>	<b>1</b>
<b>INTRODUCTION . . . . .</b>	<b>1</b>
<b>METHOD OF ANALYSIS . . . . .</b>	<b>4</b>
Geometry Definition of the Orbiter . . . . .	4
The Structural Model . . . . .	5
Aerodynamic Representation . . . . .	5
Static stability analysis . . . . .	5
Dynamic stability analysis . . . . .	8
<b>RESULTS AND DISCUSSION . . . . .</b>	<b>8</b>
Static Stability and Elastic Deformations . . . . .	8
Linear theory and method . . . . .	8
Force correction method . . . . .	8
Pressure correction method . . . . .	9
Force and pressure correction method . . . . .	9
Dynamic Stability . . . . .	11
<b>CONCLUSION . . . . .</b>	<b>12</b>
<b>APPENDIX — AERODYNAMIC FORCE AND PRESSURE DATA INCORPORATED INTO THE LINEAR THEORY SOLUTION — A FLEXSTAB CORRECTION . . . . .</b>	<b>14</b>
<b>REFERENCES . . . . .</b>	<b>29</b>
<b>TABLES . . . . .</b>	<b>30</b>
<b>FIGURES . . . . .</b>	<b>33</b>



## SYMBOLS

$[A_{P\theta}]$	steady aerodynamic influence coefficient matrix (eq. 3.5-41, ref. 1)
$[A_{F\theta}]_1$	$\equiv [T_{FP}][q_c][A_{P\theta}]_1$ (eqs. 5.3-3, ref. 1)
b	semispan of a thin body
$c_p$	pressure coefficient
$\{c_p^S\}^{iso}$	matrix of isolated thickness induced pressure coefficient
$\{c_p^V\}^{int}$	matrix of interference coefficients relevant to vortex interference
c	chord
$\bar{c}$	mean aerodynamic chord
{D}	matrix of leading-edge panel force per unit panel span
$F_x, F_y, F_z$	components of aerodynamic force along Body Axes
$\{f_T^A\}^{iso}$	matrix of aerodynamic force components induced by thickness but not including thickness interference forces
$\{f_T^A\}^{int}$	matrix of interference aerodynamic force components induced by thickness
$I_{XX}, I_{YY}, I_{ZZ}, I_{XZ}$	components of moment of inertia about Body Axes
$\begin{bmatrix} & \\ I & \end{bmatrix}$	identity matrix
M	Mach number
$M_x, M_y, M_z$	rolling, pitching, and yawing moments about Body Axes
$\begin{bmatrix} & \\ \Delta M_t & \end{bmatrix}$	matrix of Mach number variation for calculating the effect of isolated thickness on body forces;
	$\begin{bmatrix} & \\ \Delta M_t & \end{bmatrix} \equiv \frac{M_\infty}{U} [ \bar{Y}_t ] R$
P	rate of roll
$\hat{P}$	$= \frac{Pb}{2U}$ , nondimensionalized P

$[P_\theta]$	structural transformation matrix -- from nodal displacement components to aerodynamic control point rotations (eq. 4.2-101, ref. 1)
$Q$	rate of pitch
$\hat{Q}$	$= \frac{Qc}{2U}$ , nondimensionalized $Q$
$\bar{q}$	dynamic pressure apparent to Reference Axis System (eqs. 2.3-75, ref. 1)
$\bar{q}_\infty$	dynamic pressure apparent to the Fluid Axis System (eqs. 2.3-74, ref. 1)
$\nabla \bar{q}_t \downarrow$	dynamic pressure distribution formed as [ $\bar{q}_c$ ] but does not include the coordinates of the slender body mean interference surface panels
$\nabla \bar{q}_c \downarrow$	dynamic pressure distribution referring to the aerodynamic centroids of all aerodynamic segments (i.e., slender body centerline segments, slender body mean interference surface panels, and thin body mean surface panels) (eq. 3.5-54, ref. 1)
$R$	rate of yaw
$\hat{R}$	$= \frac{Rb}{2U}$ , nondimensionalized $R$
$S_w$	wing area
$[SD^S]$	transformation matrix -- from a Stability Axis System to a Body Axis System (eqs. 5.3-44, ref. 1)
$U$	X-component of the translational velocity of the Body Axis System relative to the Inertial Axis System
$X, Y, Z$	Reference Axis System (fig. 1)
$X_B, Y_B, Z_B$	Body Axis System (fig. 1)
$\nabla \bar{Y}_c \downarrow$	matrix of the coordinates of the aerodynamic centroids of all aerodynamic segments (i.e., slender body centerline segments, slender body mean interference surface panels, and thin body mean surface)
$\nabla Y_t \downarrow$	matrix of the coordinates of the aerodynamic centroids of all aerodynamic segments excluding the coordinates of the slender body mean interference surface panels
$\alpha$	angle of attack

$\beta$	sideslip angle
$\gamma$	flight path angle
$\delta$	elevon angle
$\delta_a$	aileron angle
$\delta_e$	elevator angle ( $\delta$ is substituted in place of $\delta_e$ in the longitudinal stability computation)
$\delta_r$	rudder angle
$\theta$	pitch attitude
$\{\theta^*\}$	matrix of elastic rotations at control points
$\phi$	angle of bank
$\{\psi_\alpha\}$	matrix of flow incidence due to angle of attack
$\{\psi_\beta\}$	matrix of flow incidence due to sideslip
$\{\psi_{\delta_a}\}$	matrix of flow incidence due to aileron deflection
$\{\psi_{\delta_e}\}$	matrix of flow incidence due to elevator deflection
$\{\psi_{\delta_r}\}$	matrix of flow incidence due to rudder deflection
$\{\psi_c\}$	matrix of flow incidence arising from camber shape
$\{\psi_M\}$	matrix of flow incidence arising from aircraft motion and control surface deflections
$\{\psi_P\}$	matrix of flow incidence due to roll rate
$\{\psi_Q\}$	matrix of flow incidence due to pitch rate
$\{\psi_R\}$	matrix of flow incidence due to yaw rate

Subscripts:

$B$	quantity referring to Body Axis System
$E$	quantity relevant to a flexible aircraft
$E'$	quantity associated with elastic increment
$I$	$I$ th thin body
$i$	quantity at $i$ th panel

JK	quantity of Kth centerline segment of a slender body J
R	quantity relevant to a rigid aircraft
X, Y, Z	X, Y, Z component of the quantity in Reference Axis System
1	quantity evaluated in the reference flight condition
$\infty$	quantity referred to free stream

**Superscripts:**

A	quantity relevant to aerodynamic forces
[ ] <sup>T</sup>	transpose of matrix
$C_L$	lift coefficient, $\frac{\text{lift}}{\bar{q}_1 S_w}$
$C_D$	drag coefficient, $\frac{\text{drag}}{\bar{q}_1 S_w}$
$C_m$	pitching-moment coefficient, $\frac{\text{pitching moment}}{\bar{q}_1 S_w \bar{C}}$
$C_{m\dot{\alpha}}$	$= \frac{\partial C_m}{\partial \left( \frac{\dot{\alpha} \bar{C}}{2U_1} \right)}$ , variation of pitch-moment coefficient with rate of change of angle of attack
$C_{m_q}$	$= \frac{\partial C_m}{\partial \left( \frac{q \bar{C}}{2U_1} \right)}$ , variation of pitch-moment coefficient with pitch rate
$C_p$	lifting-pressure coefficient

STATIC AND DYNAMIC STABILITY ANALYSIS OF  
THE SPACE SHUTTLE VEHICLE-ORBITER

Wei J. Chyu, Ralph K. Cavin,\* and Larry L. Erickson

Ames Research Center

SUMMARY

The longitudinal static and dynamic stability of a Space Shuttle Vehicle-Orbiter (SSV Orbiter) model is analyzed using the FLEXSTAB computer program. Nonlinear effects are accounted for by application of a correction technique in the FLEXSTAB system; the technique incorporates experimental force and pressure data into the linear aerodynamic theory. A flexible Orbiter model is treated in the static stability analysis for the flight conditions of Mach number 0.9 for rectilinear flight (1 g) and for a pull-up maneuver (2.5 g) at an altitude of 15.24 km. Static stability parameters and structural deformations of the Orbiter are calculated at trim conditions. For the dynamic stability analysis, the characteristics of damping in pitch are investigated for a Mach number range of 0.3 to 1.2. The calculated results for both the static and dynamic stabilities are compared with the available experimental data. These comparisons show that it is necessary to use the correction technique due to the nonlinearity. The calculated results indicate that the elevon effectiveness and the longitudinal stability are lower for the elastic Orbiter model than for the rigid model. The g effect on the trim solutions is significant for both the rigid and flexible models. Calculated pitch damping is in good agreement with the experimental results.

INTRODUCTION

Aeroelastic effects were neglected in most aircraft stability analyses until recently when the large transonic and supersonic aircraft posed difficult stability problems. The apparent static stability characteristics of these aircraft are drastically affected by the elastic deformations of their low-aspect ratio thin wings and slender fuselages. Further, the dynamic stability is significantly affected by the dynamics of the structure through unsteady aerodynamic coupling between the rigid body and the structural motions. For these aircraft, a mathematical model based fundamentally on the dynamics of a flexible body is required to predict static and dynamic stability. To meet this demand, a system of digital computer programs known as the FLEXSTAB system was recently developed (ref. 1).

The distinctive features of the FLEXSTAB system are its ability to evaluate static and dynamic stability, trim state, inertial and aerodynamic

---

\*Texas A&M University, College Station, Texas 77843.

loading, and elastic deformations of aircraft configurations at subsonic and supersonic speeds. The FLEXSTAB system was used previously in the analysis of such modern aircraft configurations as the Boeing 707 (ref. 2) and the YF-12A (ref. 3). Because the FLEXSTAB system imposes a restriction of small disturbances to airflow by the configurations, the configuration of the Boeing 707 airplane, which falls within this restriction, results in good agreement between the theory and the experiments for the pressure distribution on the wing. However, a complex configuration like that of the YF-12A aircraft results in significant discrepancies between the theoretical results, wind-tunnel data, and flight-test data, particularly in the region of the forebody chine and the outboard wing. The discrepancies are attributed to the vortex flow in the forebody chine, a flow that the linear aerodynamic theory within the FLEXSTAB cannot simulate.

The purpose of this report is to describe the technique of applying the FLEXSTAB system to the static and dynamic stability analyses of a flexible Space Shuttle Orbiter configuration. The SSV Orbiter configurations feature a bulky fuselage blended with a swept thick wing and forebody chine (ref. 4). This type of configuration, as that of the YF-12A, is likely to cause flow separation on most of its surface and vortex flows emanating from the leading edge of the wing. The exact linear theory alone cannot treat this kind of nonlinear flow problem. The correction approaches available within FLEXSTAB are thus used in the static stability analysis by incorporating the experimental aerodynamic data into the linear aerodynamic theory. The linear aerodynamic and structural theories are used with the wind-tunnel results for the rigid model to predict the aeroelastic effects of the actual airframe configuration, and thus to give improved predictions of the actual aircraft stability and elastic deformation. For the dynamic analysis, the characteristics of damping in pitch are investigated using the linear theory of FLEXSTAB.

For the static stability analysis the following analytical methods in the FLEXSTAB are used:

1. Linear aerodynamic and structural theories — linear theory
2. Implementation of experimental aerodynamic forces and moments into the linear-theories in (1) but using program-computed pressures — force correction
3. Implementation of experimental pressures into the linear-theories in (1) but using program-computed forces and moments (based on the experimental pressures) — pressure correction
4. Implementation of experimental aerodynamic forces, moments, and lifting pressures into the linear theories in (1) — force and pressure correction

The simple approach is to use all linear theory as in Method 1. When this was done it was discovered that the FLEXSTAB model did not always give good results for the pressure distributions or for the force and moment coefficients, the zero alpha coefficients being particularly poor. In addition, at the relatively high angle of attack at which trim occurs, the wind-tunnel

data exhibit a nonlinear variation with angle of attack. As mentioned above this nonlinear behavior cannot be predicted by the linear theory of FLEXSTAB. Consequently, Methods 2-4 were tried in an attempt to improve the linear FLEXSTAB results.

As shown in reference 1 (vol. I, pp. 5-21) and also in the appendix, the flexible aircraft aerodynamic derivatives in the linear theory analysis are composed of the sum of two quantities — the rigid aircraft aerodynamic derivatives and an increment due to static aeroelasticity. In Methods 2-4, which utilize nonlinear wind-tunnel force and pressures, this separation into a rigid component and an aero-elastic increment is still assumed to be valid.

Because of the discrepancies between the nonlinear experimental data and the linear theoretical results of Method 1, this method cannot be expected to predict an accurate trim solution for either the rigid or elastic case. Since the trim solution for the rigid case depends only on the integrated effects of the pressures (i.e., the pressure distribution can be wrong so long as the forces and moments are correct), Method 2, which replaces the theoretically computed forces and moments with nonlinear wind-tunnel values, is appropriate for the trim solution of a rigidly modeled vehicle. Since the aeroelastic increments in the flexible vehicle analysis depend explicitly on the pressure distribution, Method 2 would not be appropriate for the flexible aircraft analysis unless the pressure distribution is correctly predicted by the method. The incorrect pressure distribution that results from using Methods 1-2 thus will in general produce incorrect aeroelastic increments, even though correct wind-tunnel values are used for the rigid components of the force and moment coefficients. Thus, Method 3 was tried so that the calculated aeroelastic increments would be based on the measured pressures of the rigid wind-tunnel model rather than on the incorrect theoretical pressures by Methods 1-2.

It was expected that the rigid components of the aerodynamic force and moment coefficients computed by FLEXSTAB from these experimental pressures would be in good agreement with the wind-tunnel results. Such was not the case, however, and there is no satisfactory explanation for the disagreement. Consequently, Method 4 was used. In Method 4, the experimental pressures are used for computing the aeroelastic increments, and the wind-tunnel force and moment coefficients were used (in place of the rigid component values FLEXSTAB computes from the experimental pressures) for computing the rigid aerodynamic derivatives and trim solution.

It should be noted that the effect of the pressure correction in Method 3 is to make corrections to the theoretical pressure terms which are present in both the rigid and elastic components of the theoretical aerodynamic force. As both the force and pressure are introduced in the correction (Method 4), the effect of pressure correction is only on the elastic increment as its effect on the rigid component is superseded by the force correction.

The main context of this report presents the techniques of applying the FLEXSTAB to the Space Shuttle Orbiter configuration. The analytical description of the technique is summarized in the appendix which is based on the

voluminous FLEXSTAB program documents. The correction method is also derived in the appendix since there is a lack of clarity in the documents on the correction method.

The computations for the longitudinal static stability study are made for two flight conditions: a rectilinear flight (1 g) and a pull-up maneuver (2.5 g), both at Mach number 0.9 and an altitude of 15.24 km. This flight condition is specifically chosen for the static analysis, because at this condition the greatest aeroelastic effects are observed within the Mach numbers investigated. In the dynamic stability analysis, a rigid Orbiter is treated using linear aerodynamic theory (ref. 1). The characteristics of damping in pitch, as given by the parameters  $C_{m\alpha}$  and  $C_{mQ}$  are investigated for a Mach number range of 0.3 to 1.2. Throughout this report, the analytical results are compared with available experimental data.

## METHOD OF ANALYSIS

### Geometry Definition of the Orbiter

The Orbiter configuration (ref. 4) is described by using three types of component bodies in the Geometry Definition Program of the FLEXSTAB: (1) a slender body, (2) a thin body, and (3) an interference body (fig. 1). The Orbiter fuselage is represented by a slender body of revolution whose cross-sectional areas are the same as those of the fuselage. The line singularities representing the fuselage are extended downstream from the physical fuselage (order of 100 fuselage lengths). This procedure was adopted to more accurately represent the actual flow field aft of the blunt-base fuselage (ref. 1, pp. 3-101, vol. IV, and/or vol. II). The camber line for the slender body is the locus of the area centroids of fuselage. The wing is represented by a thin body which is essentially the projection of the wing planform onto a mean plane. This projected wing plane is subdivided into panels with which FLEXSTAB associates appropriate aerodynamic singularities and control points (fig. 1). The 3.5° dihedral of the wing was neglected in order to ensure compatibility with structural data. Wing camber and thickness effects are described by the wing airfoils (fig. 2) at various spanwise stations. The blunt airfoil trailing edge of the Orbiter has been replaced with a sharp trailing edge in keeping with a FLEXSTAB requirement. The Orbiter vertical tail is excluded in the geometry description. Studies of the rigid case indicate that the omission of the tail and the wind dihedral angle in the geometry definition has little effect on the results of the longitudinal stability analysis. Interference effects due to wing-induced downwash on the fuselage are approximately accounted for by introducing an interference body of polygonal cross section (fig. 1). The vortex singularities associated with the panels on the interference shell are used to account for the normal component of flow induced by the wing. In defining the Orbiter geometry the body flap was not incorporated into the present analysis because the flap would intersect the interference body in a manner which cannot be accommodated by the existing FLEXSTAB.

A rather lengthy sequence of computer runs was conducted for the rigid vehicle in an effort to determine what combinations of geometric parameters result in aerodynamic stability data that more closely correlate with available wind-tunnel data. The effort involves changing shape and locations of the interference body, and modifying the paneling scheme and singularity distribution to obtain an improved estimate for lift and moment-curve slopes. It results in the Orbiter geometry shown in figure 1, which consists of 50 control points equally spaced along the fuselage, 98 finite-element panels on the wing, and 120 panels on the interference body. Computations with a larger number of finite-element panels and more densely defined airfoil than that shown in figures 1 and 2 were also tried but they yielded no further convergence in the numerical results.

### The Structural Model

The External Structural Influence Coefficient (ESIC) program was used to couple FLEXSTAB to externally generated structural and inertia representations for the Orbiter. The structural model was provided by the Structures Group of Rockwell International Space Division. The model was a reduction of a large finite-element model of the Orbiter existing in Rockwell's computer program, ASKA. An interface was created between the output data tape obtained from ASKA and subprogram ESIC of the FLEXSTAB system.<sup>1</sup>

The model provided by Rockwell International has a very dense nodal representation for the wing; it contains 200 nodes, each of which possesses the Z degree of freedom (fig. 3). In the leading-edge area of the wing, where no structural nodes are available, the FLEXSTAB interpolates the structural properties of nearby nodes to the aerodynamic centroid of the proper aerodynamic model.

The representation of the fuselage structure involves difficulties in representing, by a single line of nodes located along the centerline of the fuselage, the structural asymmetry induced in the fuselage by the upper "clam shell" cargo doors. The fuselage structural model provided by Rockwell International contains nine structural nodes each possessing X and Z degrees of freedom. The necessary structural data for the rigid Orbiter computation are shown in figure 1, and are input directly to the FLEXSTAB program.

### Aerodynamic Representation

*Static stability analysis-* One of the major concerns during the course of this study was to select an aerodynamic representation which, together with an appropriate Orbiter geometry definition, accounts for nonlinear flow effects on the aerodynamic stability. It is evident that the nonlinear flow phenomena, such as the flow separation on most of the Orbiter surface and the vortex flows on the swept wing, cannot be described mathematically by the linear aerodynamic theory within the FLEXSTAB. However, the linear theory solutions

---

<sup>1</sup>The interface was prepared by A. R. Curtis, Lockheed-California Company.

are of value in providing general aerodynamic trends; they also provide theoretical reference to which a correction on the deficiency of the theory can be made. A sequence of computations was conducted applying the following methods of aerodynamic representation:

1. Linear aerodynamic and structural theories — linear theory

2. Implementation of experimental aerodynamic forces and moments into the linear theory solution of (1) but using program computed pressures — force correction

3. Implementation of experimental lifting pressures into the linear-theories solution of (1) but using program-computed forces and moments (based on the experimental pressures) — pressure correction

4. Implementation of experimental aerodynamic forces, moments and lifting pressures into the linear theory solution of (1) — force and pressure correction

The analytical details of the above methods are described in the appendix of this report; thus only the summary of the correction techniques and the computational procedures are described in this section. The experimental forces and moments ( $C_L$ ,  $C_D$ ,  $C_m$ ) data are put into tabular forms as a function of angle of attack and elevon deflection, as shown in figure 4, and are provided as inputs to the FLEXSTAB. The experimental lifting pressures are implemented into the FLEXSTAB by representing the pressures on both the wing and fuselage by a linear function of the angle of attack; that is,

$$\Delta C_{p_i}^{WT} = \Delta C_{p_{i_0}}^{WT} + \Delta C_{p_{i_0}}^{WT} \alpha \quad (1)$$

where the subscript  $i$  denotes the  $i$ th body station, and superscript WT denotes wind-tunnel data. The coefficients  $\Delta C_{p_{i_0}}^{WT}$  and  $\Delta C_{p_{i_0}}^{WT} \alpha$  are chosen so

that the nonlinear experimental data for  $0^\circ < \alpha < 14.5^\circ$  are approximated by the analytically fitted expression (1) in the range of selected parameters; namely,  $\alpha$  in the present consideration. The choice of this range of  $\alpha$  is justified if the calculated trim angles fall within the range. The optimal linear approximations, as those shown in figure 5, are applied to 50 fuselage stations and to 98 wing stations.

In the approach for implementing the experimental data into the linear theory, the separation of the aerodynamic derivatives into a rigid component and into an aeroelastic increment, as in the linear theory analysis, is still assumed to be valid; that is,

$$\begin{bmatrix} F_{XB\lambda} \\ F_{ZB\lambda} \\ M_{YB\lambda} \end{bmatrix}_E = \begin{bmatrix} F_{XB\lambda} \\ F_{ZB\lambda} \\ M_{YB\lambda} \end{bmatrix}_R + \begin{bmatrix} \Delta F_{XB\lambda} \\ \Delta F_{ZB\lambda} \\ \Delta M_{YB\lambda} \end{bmatrix}_E, \quad (2)$$

where  $\lambda$  represents  $\alpha$ ,  $\delta_e$ , or  $Q$  in the case of longitudinal analysis. The effect of the experimental aerodynamic force and moment implementation (in Method 2 or 4) is on the terms  $[F_{XB\lambda}, F_{ZB\lambda}, M_{YB\lambda}]_R^T$  only, which are interpolated from the tabulated input data. The objective of the force implementation in Methods 2 and 4 is to force the trim solutions to be accurately correlated with the wind-tunnel data. Since the trim solution for the rigid case depends only on the integrated effects of the pressures, the force correction allows the experimental force data to represent global effects of the nonlinear flow on the rigidly modeled aircraft (i.e., the rigid term in eq. (2)).

The effect of the pressure implementation in Method 3 is to make corrections to both the theoretically calculated rigid and elastic terms in the right side of equation (2) to account for the local nonlinear flow effects.

If the experimental force and pressure implementations are applied to the FLEXSTAB (Method 4) simultaneously, the effect of the pressure is on the elastic increment term only while the effect of the pressure on the rigid term is superseded by the force data that are allowed to represent completely the global effects or the rigid term in equation (2). The trim solutions and the calculated pressure distribution on a flexible aircraft thus have the combined effects from the force and pressure data measured on the rigid wind-tunnel model and the results of the theoretically calculated elastic increment. The objective of this scheme is to force the trim solutions to be accurately correlated with the wind-tunnel data, and allow the experimental forces and pressures to represent both the global and the local effects of the nonlinear flow while the elastic effects are calculated theoretically. Since the linear theory alone cannot treat the nonlinear flow phenomena which are inherent with the Orbiter configuration, an effort was focused on seeking a correction approach in which the linear theory solutions are implemented with experimental data. Methods 2 and 3 are investigated before Method 4 in order to find an approach by which the linear theory is integrated with less experimental data than is Method 4 and yet one capable of predicting the remaining experimental data correctly. Although Methods 2 and 3 are shown to be inapplicable to the Orbiter, it should be noted that their techniques (appendix) are valid and may be applied to other aircraft configurations. The application of the above correction techniques to a realistic aircraft has never been reported. This is probably due to the lack of experimental data and at least partially, to the nature of the technique, which requires a time-consuming effort to prepare the required correction data to make the data compatible with the FLEXSTAB system. This report presents the results of computations based on the linear theory and/or the linear theory implemented with experimental data.

*Dynamic stability analysis-* The linear aerodynamic theory in FLEXSTAB (ref. 1) is used to compute the pitch parameters,  $C_{m\hat{\alpha}}$  and  $C_{m\hat{Q}}$  for a rigid Orbiter in the Mach number range of 0.3 to 1.2.

## RESULTS AND DISCUSSION

### Static Stability and Elastic Deformation

Four analytical methods were used to determine which method gives static stability and the lifting pressures comparable with experimental data, and thus the one that can be used to estimate correctly the aeroelasticity effect and the aircraft deformation. The results of computations based on the following methods are presented. All of the results are for the Orbiter configuration depicted in figures 1 and 2. The computation for the rigid Orbiter model is compared with the wind-tunnel data for Mach number 0.9 at  $\alpha = 10^\circ$  and  $\delta = 0^\circ$ .

*Linear theory method-* The calculated lifting pressures are shown in figure 6. On the fuselage surfaces at  $x = 13$  to  $25$  m where potential-like flow exists due to the straight contour of the fuselage, the calculated pressure is in good agreement with the experiment. On the nose and tail regions of the fuselage, discrepancies of pressures are noted between the calculated and the experimental results, but the qualitative trend of the calculated pressure distribution is similar to that measured on the wind-tunnel model. This indicates that the pressure discrepancies are strongly associated with the nonlinear flow occurring on the nose and tail regions of the fuselage. The lifting pressures on the wing at various spanwise stations are shown in figures 7(a)-(g). It is noted that the agreement between the calculated pressure and the measurements is fairly good in the midchord region of the inboard wing section. The agreement, however, is poor in the region near the leading and the trailing edges and also on the outboard wing section. These discrepancies are attributable to vortex flow on the leading-edge region and on the outboard section of the wing, and to flow separation near the trailing-edge region.

The zero aerodynamic coefficients calculated by using linear theory are shown in table 1. The calculated  $C_{L_0}$  and  $C_{m_0}$  are comparable to the experimental results within an order of magnitude, whereas the calculated  $C_{D_0}$  shows a small drag relative to the experimental result. The calculated static stability coefficients are shown in table 2. The comparison of the results of the linear theory (Method 1) with that of Methods 2 or 4 (which are essentially interpolated from the wind-tunnel data) shows that the agreement between the results from the linear theory and experiments is generally good, within an order of magnitude. The agreements in  $C_{L\hat{Q}}$  and  $C_{m\hat{Q}}$  are excellent.

*Force correction method-* This method provides trim solutions for which the trim angle is calculated in an iterative manner from the tabulated experimental data. The lifting pressures are then calculated using the linear

theory for the trim angles. The computation results in trim angles  $\alpha = 9.5^\circ$  and  $\delta = 7.4^\circ$ , and the corresponding pressures shown in figures 8 and 9. These results are compared with those from the linear theory and experiments which specify  $\alpha = 10^\circ$  and  $\delta = 0^\circ$ . It shows that the effect of the elevon deflection is to increase the pressure on the tail region of the fuselage and on the trailing-edge region of the wing. However, this method still does not predict accurately the experimental pressures (fig. 9). It is obvious that the linear aerodynamic representation of the actual flow by this method is poor and thus Method 2 would not be a good choice for studying the aeroelastic effects.

*Pressure correction method-* Incorporation of the experimental pressure data into FLEXSTAB through the use of equation (1) results in the distributions of pressures given in figures 6 and 7. The match of the results of this scheme and those of experiment is excellent, indicating that the experimental pressures are correctly incorporated into the linear theory solution. The aerodynamic derivative results from this method are shown in table 3 and are compared with those interpolated from experiments. It is noted that the results for  $C_{L_0}$ ,  $C_{L\hat{\delta}}$ ,  $C_{D\hat{Q}}$ , and  $C_{M\hat{Q}}$  are in good agreement. However, the disagreement of  $C_{m_0}$ ,  $C_{m_\delta}$ ,  $C_{L_\delta}$  is rather contradictory to the fact that these parameters are related to the aerodynamic forces that are mathematically integrated from the experimental pressures and thus should agree with the measured forces and moments. Since  $C_{m_0}$ ,  $C_{m_\delta}$ , and  $C_{L_\delta}$  are associated with the elevon it leads to the belief that the disagreement is attributable to the Orbiter elevon which is geometrically defined in the computation differently from the wind-tunnel model; that is, the trailing-edge region of the wing is smoothed and the edge is assumed to be closed in the computation whereas the Orbiter actually has a blunt trailing edge with thickness varied from 7.62 to 17.65 cm. This method is considered inappropriate for use in the aeroelasticity study since some of the aerodynamic forces and moments are still not correctly predicted.

*Force and pressure correction method-* Because of the foregoing results it was decided that the linear theories implemented with force and pressure corrections would be used to compute the aeroelasticity effect and the Orbiter structural deformation. Table 4 shows the calculated results of trim solutions including the aerodynamic coefficients and derivatives for the rigid and elastic cases. The comparison of the rigid and elastic cases, both at the same flight condition (1 g or 2.5 g), indicates that the aeroelastic effects are negligibly small. However, it is noted that:

1. A slightly larger elevon trim angle is required in the elastic case than in the rigid case to account for the aeroelastic effects.
2. As the Orbiter is assumed to be flexible,  $C_{m_\alpha}$  is increased but  $C_{m_0}$  is decreased. This results in practically no change between the rigid and the elastic cases at trim condition in the longitudinal stability,  $C_m$ .
3. The elevon effectiveness in controlling lift ( $C_{L_\delta}$ ) and longitudinal stability ( $C_{m_0}$ ) is decreased when the Orbiter is assumed flexible.

4. The aeroelastic effect on lift and drag coefficients is negligibly small, although a small amount of loss in lift is evidenced by a small decrease in  $C_{L_0}$  or  $C_{L_\alpha}$ .

5. The negligibly small aeroelastic effect on  $C_{m_Q}$  and  $C_{m_\alpha}$  indicates that the dynamic stability study may be confined to the rigid case only.

The effects of g loading on the trim conditions as observed from table 4 are as follows for both the rigid and elastic cases:

1. Higher g-load condition requires higher trimming of angles  $\alpha$ ,  $\theta$ , and  $\delta$ .

2. The zero derivatives  $C_{L_0}$  and  $C_{m_0}$  are not affected by the increase of g-loading whereas the derivatives  $C_{L_\alpha}$  and  $C_{m_\alpha}$  are greatly affected.

Thus the Orbiter at high g-load condition loses its effectiveness in lift and longitudinal stability control.

3. The effect of g-load change on  $C_{D_0}$  and  $C_{D_\alpha}$  is negligibly small.

4. The derivatives of  $C_L$ ,  $C_D$ , and  $C_m$  with respect to  $\hat{Q}$  and  $\delta$  are practically independent of g-load condition.

Figure 10 shows the estimated pressure distributions on the fuselage under trim condition in the two flight cases. The pressure increment due to aeroelastic effect is negligibly small so that figure 10 actually represents the results of both the rigid and elastic models. The results are compared with the experimental data for which  $\alpha$  and  $\delta$  are  $10^\circ$  and  $0^\circ$ , respectively. The estimated pressures for the trim 1-g flight case ( $\alpha = 9.5^\circ$ , and  $\delta = 7.6^\circ$ ) agrees with the experiment except near the tail ( $x = 28$  m) where the estimated pressure shows a peak indicating the interference from the elevon deflection ( $\delta = 7.6^\circ$ ). On the upstream region of the fuselage ( $x = 0$  to  $10$  m) the pressure varies greatly due to the abrupt change in camberline slopes.

In the midsection of the fuselage there still exists appreciable pressure variation which indicates that the pressure is recovering from the abrupt pressure change in the forebody. Figure 10 also shows that the pressure is appreciably higher in the 2.5-g flight case than in the 1-g flight case.

Figure 11 shows the calculated pressure distribution on the wing when the Orbiter is in the trim condition. Since the calculated trim angles ( $\alpha = 9.5^\circ$  and  $\delta = 7.6^\circ$ ) for the 1-g load condition are not exactly the same as those of experiment ( $\alpha = 10^\circ$  and  $\delta = 0^\circ$ ), the computation shows a pressure rise on the elevon area. The pressure rise due to elevon deflection covers only the elevon area on the inboard section of the wing. On the outboard section of the wing the pressure rise is extended farther upstream of the elevon area. The trend of the chordwise pressure distribution on the wing is similar for both the 1-g and 2.5-g load conditions. However, in the outboard region of the wing where the semispan is larger than 44.20%, the high angle of attack in the 2.5-g flight condition gives rise to a sudden pressure increase in the

leading-edge region. This pressure rise produces a large pressure differential between the leading-edge and midchord region of the wing and thus causes total twist on the wing outboard section. On the wing near the 27.1% semispan a significant pressure rise occurs at  $x/c = 0.25$ , due to the interference of the pressure rise on the adjacent fuselage.

The results of the estimated fuselage displacements are shown in figure 12 for 1-g and 2.5-g load conditions. The fuselage appears to deform in the inverted "U-shape" with maximum displacement occurring at the downstream end of the fuselage. It is noticed that a rather sharp inflectional displacement occurs on the fuselage at  $x = 19$  m and 27 m. The inflection at  $x = 27$  m is attributed to the structural discontinuity at that location where the cargo bay meets the fuselage. The inflection at the middle region of fuselage,  $x = 19$  m, is caused by the first mode bending of the fuselage structure.

Figures 13(a)-(i) shows the estimated wing structural displacements at span locations corresponding to those of the pressure distribution shown in figure 10. The figures display increasingly larger displacements toward the outboard regions of the wing. A very little twist to the wing is observed for the 1-g load condition. However, in the 2.5-g maneuver case, a twist occurs on the trailing-edge region of the wing, accounting for the pressure rise due to the elevon deflection. A twist also occurs toward the leading edge of the outboard region of the wing with semispan larger than 61.28%, accounting for the sudden pressure rise due to the large angle of attack in the 2.5-g flight condition. The twists that occurred in the leading- and trailing-edge regions are in the opposite directions and thus result in a concave-shaped displacement on the outboard region of the wing. Twist does not occur on the leading edge portion of the inboard region of the wing except near the extreme inboard section of the wing (27.1% semispan), where a twist occurs near the leading edge due to interference from the pressure rise on the adjacent fuselage.

#### Dynamic Stability

The characteristics of the pitch damping of a rigid Orbiter model was investigated using the linear theory approach of the FLEXSTAB (ref. 1). Figure 14(a) shows the calculated pitch damping represented by  $C_{m\hat{\alpha}}$  and  $C_{m\hat{Q}}$  in the Mach number range of 0.3 to 1.2. The corresponding  $C_{m\hat{\alpha}} + C_{m\hat{Q}}$  are shown in figure 14(b) together with the experimental results (ref. 5). The following information on the damping characteristics can be drawn from figure 14:

1. The calculated  $C_{m\hat{\alpha}} + C_{m\hat{Q}}$  is in good agreement with the experimental results.
2. The negative value of  $C_{m\hat{\alpha}} + C_{m\hat{Q}}$  indicates that the Orbiter configuration possesses a stable pitch damping at subsonic and supersonic speeds.

3. As the Mach number is increased from 0.3 to 0.8 the value of  $C_{m\hat{\alpha}} + C_{m\hat{Q}}$  is decreased, indicating that the damping is increased with increasing subsonic Mach number. This increased stable condition is attributed to the decrease in both terms  $C_{m\hat{\alpha}}$  and  $C_{m\hat{Q}}$ , as shown in figure 14(a). As the Mach number is increased to 1.2,  $C_{m\hat{\alpha}} + C_{m\hat{Q}}$  is increased, indicating that the Orbiter becomes less stable in pitch damping with increasing supersonic speed. This less stable condition is attributed to the increase from 0.85 to 1.45 of the term  $C_{m\hat{\alpha}}$ .

## CONCLUSIONS

The FLEXSTAB analysis of the longitudinal stability of a Space Shuttle Vehicle-Orbiter model discloses the following.

1. Experimental aerodynamic force and pressure correction to the linear theory is required in the static stability analysis to account for the non-linear aerodynamics associated with the Orbiter configuration and thus to give an improved prediction of the aeroelastic effect on the stability.

2. The aeroelastic effect is small. However, it is evident that:

- a. A slightly higher elevon trim angle than that in the rigid case is required.
- b. The elevon effectiveness and the longitudinal stability are lower for the elastic Orbiter model than for the rigid model.
- c. The aeroelastic effects on the lift coefficients  $C_{L_0}$  and  $C_{L\hat{\alpha}}$  and on the drag coefficients  $C_{D_0}$  and  $C_{D\hat{\alpha}}$  are negligibly small.
- d. The calculated Orbiter deformation shows an inverted "U-shape" fuselage displacement and a concave shape displacement on the outboard region of the wing.

3. The  $g$  effect on the trim solutions is evident for both the rigid and elastic Orbiter models. The effects are:

- a. Higher  $g$  flight condition requires higher trim angles,  $\alpha$ ,  $\theta$ , and  $\delta$ .
- b. Higher  $g$  flight condition results in lower  $\alpha$  effectiveness on the lift control and longitudinal stability.
- c. The drag of the Orbiter and the derivatives ( $C_{L\hat{Q}}$ ,  $C_{D\hat{Q}}$ ,  $C_{m\hat{Q}}$ ) and ( $C_{L\delta}$ ,  $C_{D\delta}$ ,  $C_{m\delta}$ ) are independent of the  $g$  condition.

4. The dynamic stability analysis of the pitch damping,  $C_{m\alpha}^e + C_{m\dot{\alpha}}$ , for a rigid model in a Mach number range from 0.3 to 1.2 indicates that:

- a. The calculated pitch damping is in good agreement with the experimental results.
- b. The Orbiter possesses a stable pitch damping within the Mach number range investigated. However, the pitch damping stability is increased with increasing subsonic Mach number, and is decreased with increasing supersonic Mach number. This decrease in the stability is attributed to the increase of  $C_{m\dot{\alpha}}$  toward higher positive values with the increasing supersonic Mach number.

Ames Research Center

National Aeronautics and Space Administration

Moffett Field, California 94035, November 7, 1977

## APPENDIX

### AERODYNAMIC FORCE AND PRESSURE DATA INCORPORATED INTO THE LINEAR THEORY SOLUTION - A FLEXSTAB CORRECTION

A correction method of the FLEXSTAB by incorporating experimental aerodynamic forces and/or lifting pressure data into the solution of the linear theory is described. The objective of the method is to amend the linear theory solution to account for the nonlinear flow effects. The data to be used for such purposes can be those obtained either by experimental or analytical methods; however, in the present computation the former approach is used. The following describes first the linear theory by which the FLEXSTAB normally solves the static aeroelasticity problem and then introduces the correction method to account for the nonlinearities in the calculation of aeroelasticity effects. The developments of this correction method described in this appendix are the summary of those given in reference 1. The essentials of the correction method, described in the voluminous FLEXSTAB program are presented, and the validity of the techniques are delineated. Some mathematical formulations in FLEXSTAB are extended to improve the verification of the techniques presented in FLEXSTAB. Mathematical terms in equations not essential for showing the technique are given only for their physical significance. The detailed mathematical expression of these terms can be found in reference 1.

#### The Static Trim Problem

An aircraft in steady reference flight can be described by the following classical equations of motion:

$$\left. \begin{aligned}
 MU_1(Q_1 \tan \alpha_1 - R_1 \tan \beta_1) + Mg \sin \theta_1 &= F_{XB_1}^A + F_{XB_1}^T \\
 MU_1(R_1 - P_1 \tan \alpha_1) - Mg \cos \theta_1 \sin \phi_1 &= F_{YB_1}^A + F_{YB_1}^T \\
 MU_1(R_1 \tan \beta_1 - Q_1) - Mg \cos \theta_1 \cos \phi_1 &= F_{ZB_1}^A + F_{ZB_1}^T \\
 (I_{ZZ_1} - I_{YY_1})Q_1R_1 - I_{XZ_1}P_1Q_1 &= M_{XB_1}^A + M_{XB_1}^T \\
 (I_{XX_1} - I_{ZZ_1})P_1R_1 + I_{XZ_1}(P_1^2 - R_1^2) &= M_{YB_1}^A + M_{YB_1}^T \\
 (I_{YY_1} - I_{XX_1})P_1Q_1 + I_{XZ_1}R_1Q_1 &= M_{ZB_1}^A + M_{ZB_1}^T
 \end{aligned} \right\} \quad (A1)$$

where  $M$  denotes the aircraft mass. The components of force and couple, the last terms of equation (A1), produced by propulsion system are assumed to be linear functions of the thrust  $T_1$ , for example,  $M_{YB_1}^T = M_{YB_1}^T T_1$ . The present study treats the reentry flight problem assuming  $T_1 = 0$ .

The aerodynamic forces are assumed to be linear functions of the aircraft motion  $\alpha_1$ ,  $\beta_1$ ,  $P_1$ ,  $Q_1$ ,  $R_1$ , and the control surface setting,  $\delta e_1$ ,  $\delta a_1$ , and  $\delta r_1$ .

$$\left. \begin{aligned} F_{XB_1}^A &= F_{XB_0}^A + F_{XB_\alpha}^A \alpha_1 + F_{XB_Q}^A Q + F_{XB_{\delta e}}^A \delta e_1 \\ F_{YB_1}^A &= F_{YB_\beta}^A \beta_1 + F_{YB_P}^A P_1 + F_{YB_R}^A R_1 + F_{YB_{\delta a}}^A \delta a_1 + F_{YB_{\delta r}}^A \delta r_1 \\ F_{ZB_1}^A &= F_{ZB_0}^A + F_{ZB_\alpha}^A \alpha_1 + F_{ZB_Q}^A Q_1 + F_{ZB_{\delta e}}^A \delta e_1 \\ M_{XB_1}^A &= M_{XB_\beta}^A \beta_1 + M_{XB_P}^A P_1 + M_{XB_R}^A R_1 + M_{XB_{\delta a}}^A \delta a_1 + M_{XB_{\delta r}}^A \delta r_1 \\ M_{YB_1}^A &= M_{YB_0}^A + M_{YB_\alpha}^A \alpha_1 + M_{YB_Q}^A Q_1 + M_{YB_{\delta e}}^A \delta e_1 \\ M_{ZB_1}^A &= M_{ZB_\beta}^A \beta_1 + M_{ZB_P}^A P_1 + M_{ZB_R}^A R_1 + M_{ZB_{\delta a}}^A \delta a_1 + M_{ZB_{\delta r}}^A \delta r_1 \end{aligned} \right\} \quad (A2)$$

Equation (A1) contains 12 parameters ( $U_1$ ,  $V_1$ ,  $W_1$ ,  $P_1$ ,  $Q_1$ ,  $R_1$ ,  $\phi_1$ ,  $\theta_1$ ,  $T_1$ ,  $\delta e$ ,  $\delta a$ , and  $\delta r$ ), 6 of which need to be specified; the remaining unspecified parameters are solved from the six equations of motion. In the present computation, six parameters —  $U_1$ ,  $P_1$ ,  $Q_1$ ,  $R_1$ ,  $\phi_1$ ,  $T$  — are specified in which  $T = 0$  is assumed for the reentry flight. For a steady pull-up with load factor  $n$ ,  $Q$  is calculated by using  $Q = (n - 1)g/U$ . The equation of motion is solved for the trim condition by the FLEXSTAB using Newton's iteration method.

The FLEXSTAB has the capability of solving linear and nonlinear trim problems:

*Linear case-* Equation (A1) is linearized as follows:

$$\left. \begin{aligned} MU_1(Q_1\alpha_1 - R_1\beta_1) + Mg\theta_1 &= F_{XB_1}^A \\ MU_1(R_1 - P_1\alpha_1) - Mg \sin \phi_1 &= F_{YB_1}^A \\ MU_1(R_1\beta_1 - Q_1) - Mg \cos \phi_1 &= F_{ZB_1}^A \\ (I_{ZZ_1} - I_{YY_1})Q_1R_1 - I_{XZ_1}P_1Q_1 &= M_{XB_1}^A \\ (I_{XX_1} - I_{ZZ_1})P_1R_1 + I_{XZ_1}(P_1^2 - R_1^2) &= M_{YB_1}^A \\ (I_{YY_1} - I_{XX_1})P_1Q_1 + I_{XZ_1}R_1Q_1 &= M_{ZB_1}^A \end{aligned} \right\} \quad (A3)$$

The equation (A3) is solved using the linear aerodynamic assumption of (A2).

*Nonlinear case-* Equation (A1) is solved for two nonlinear cases:

1. Linear aerodynamics and nonlinear kinematics. In this case the linear aerodynamic force representation of (A2) is used in conjunction with equation (A1) to formulate the trim problem.

2. Wind-tunnel aerodynamics and nonlinear kinematics. In this case equation (A1) is solved with the aerodynamic force data (nonlinear) obtained by experimental or analytical methods.

The FLEXSTAB yields the following trim solution: the control surface setting ( $\delta e_1, \delta a_1, \delta r_1$ ), the angle of attack [ $\alpha_1 = \tan^{-1}(W_1/U_1)$ ], the angle of sideslip [ $\beta_1 = \tan^{-1}(V_1/U_1)$ ], and the flight-path angle ( $\gamma_1 = \theta_1 - \alpha_1$ ).

### The Linear Theory

*Linear aerodynamic equations-* Analytical expressions for the aerodynamic forces (terms on the right side of equation (A1) are presented. Aerodynamic forces for rigid and flexible aircraft are given separately so that the aeroelasticity effects can be distinguished. Aeroelastic effects from the propulsion system are not considered.

The Reference Axis System force and moment vector can be transformed into the Body Axis System by a simple sign change for each of the vector components since the two systems are colinear but oppositely directed, that is,

$$\{F_B^A\}_1 = [S]\{F_C^A\} \quad (A4)$$

where

$$\{F_B^A\}_1 = [F_{XB}^A, F_{ZB}^A, M_{YB}^A, F_{YB}^A, M_{XB}^A, M_{ZB}^A]^T$$

and

$$[S] \equiv \begin{bmatrix} -1 & & & & & \\ & -1 & & & & 0 \\ & & -1 & & & \\ & & & -1 & & \\ 0 & & & & -1 & \\ & & & & & -1 \end{bmatrix}$$

The aerodynamic forces  $\{F_C^A\}$  are attributed to the local aerodynamic forces at each of the  $n$  panel segments. They can be expressed as follows:

$$\{F_C^A\}_1 = 2[\bar{\phi}^*]^T \{f^A\}_1 \quad (A5)$$

where

$$[\bar{\phi}^*] \equiv \begin{bmatrix} [\bar{\phi}_1^*] \\ \vdots \\ [\bar{\phi}_i^*] \\ \vdots \\ [\bar{\phi}_n^*] \end{bmatrix} \quad \text{and} \quad \{f_i^A\}_1 \equiv \begin{bmatrix} \{f_1^A\} \\ \vdots \\ \{f_i^A\} \\ \vdots \\ \{f_n^A\} \end{bmatrix}$$

The matrix  $[\bar{\phi}_i^*]$  is termed the rigid-body mode shape matrix and expressed as

$$[\bar{\phi}_i^*]^T \equiv \begin{bmatrix} 1 & 0 & 0 \\ 0 & 0 & 1 \\ \bar{z}_i & 0 & -\bar{x}_i \\ 0 & 1 & 0 \\ 0 & -\bar{z}_i & \bar{y}_i \\ -\bar{y}_i & \bar{x}_i & 0 \end{bmatrix}$$

$\bar{x}_i$ ,  $\bar{y}_i$ , and  $\bar{z}_i$  are the coordinates (in the Reference Axis System) of the center of pressure at the  $i$ th panel or slender body segment relative to the center of mass.

The term  $\{f_i^A\}$ , denotes the vector of the slender, interference, and thin body forces expressed in the Reference (Mean) Axis System. Based on the linear aerodynamic representation in FLEXSTAB,  $\{f_i^A\}$ , can be written as

$$\begin{aligned} \{f_i^A\}_1 = & \bar{q}_1 [T_{FT}] [TRANS_t] \bar{q}_t \sqrt{\left( \{C_p^S\}_{iso} + \Delta M_t \sqrt{\left( \frac{\partial C_p^S}{\partial M} \right)_1} \right)} \\ & + \bar{q}_1 [T_{FT}] [T_{TF}] [T_{FP}] \bar{q}_c \sqrt{\{C_p\}_1} + \bar{q}_1 [T_{FT}] [TRANS_{ID}] \bar{q}_c \sqrt{\{D\}_1} \end{aligned} \quad (A6)$$

where,

$$\{C_p\}_1 = [A_{p\theta}]_1 (\{\psi_c\}_1 + \{\theta^*\}_1 + \{\psi_M\}_1) + \{C_p^V\}_{int}^{int} \quad (A7)$$

represents the lifting-pressure coefficients. The steady flow incidence  $\{\psi_M\}_1$  can be expressed as:

$$\begin{aligned}\{\psi_M\}_1 &= \left\{\psi_{\delta_e}\right\} \delta e_1 + \left\{\psi_{\delta_a}\right\} \delta a_1 + \left\{\psi_{\delta_r}\right\} \delta r_1 + \{\psi_\alpha\} \alpha_1 \\ &\quad + \{\psi_\beta\} \beta_1 + \{\psi_p\} \frac{2}{b} \hat{P}_1 + \{\psi_Q\} \frac{2}{c} \hat{Q}_1 + \{\psi_R\} \frac{2}{b} \hat{R}_1\end{aligned}\quad (A8)$$

Physical significance of the transformation matrices in equation (A6) are described as follows:

$[T_{fT}]$  — A matrix that transforms the pressure from the local thin and slender-body axis system to the Reference Axis System (eq. 3.5-30, ref. 1).

$[TRANS_t]$  — A matrix that transforms the thickness induced pressure, that is,  $\{C_p^S\}_{iso}$ , to components of forces in the local thin and slender-body axis systems (eq. 3.5-31, ref. 1).

$[T_{TF}]$  — A matrix that transforms forces on the mean camber surface to the components expanded in local Body Axis System (eq. 3.5-32, ref. 1).

$[T_{FP}]$  — A matrix that transforms lifting pressure  $\bar{q}\{C_p\}$  on a panel element to the components of force in local thin and slender-body axis (eq. 3.5-33, ref. 1).

The various terms on the right side of equation (A6) can be given the following general interpretations:

1. First term: There are two components; one representing the effect of isolated thickness on body forces and the second representing the effect of Mach number variations on the forces induced by isolated thickness effects.

2. Second term: This term accounts for the effects of lifting pressures and interference pressure on the body forces. The lifting pressures here represent those caused by camber shape, elastic rotation, aircraft motion, and control surface deflections.

3. Third term: This term represents the components of body forces arising from leading-edge panel force.

The second term is of primary interest to the present study because, as indicated in equations (A6) to (A8), it is dependent on the problem motion variables. Note that  $\{C_p\}$ , in equation (A7), is partially computed from the operation of the steady aerodynamic influence coefficient matrix  $[A_{p0}]_1$  on the sum of camber incidence vector  $\{\psi_C\}_1$ , the motion incidence vector  $\{\psi_M\}_1$  involving aircraft rotation, and control surface deflection, and aircraft deformation  $\{\theta^*\}$ .

*Linear structural equations-* The structural displacements  $\{\delta\}_1$  are computed from the applied aerodynamic force,  $\{Q^A\}_1$ , by

$$\{\delta\}_1 = [\tilde{C}]_1 \{Q^A\}_1 \quad (A9)$$

where  $[\tilde{C}]_1$  is termed the unconstrained flexibility matrix. The deformation incidence vector  $\{\theta\}_1^*$  is related to  $\{\delta\}_1$  by

$$\{\theta^*\}_1 = [P_\theta] \{\delta\}_1 \quad (A10)$$

The airloads  $\{f_T^A\}_1$  of aerodynamic load points can be transformed to structural node forces by

$$\{Q^A\}_1 = [P_T]^T \{f_T^A\}_1 \quad (A11)$$

Substitution from equations (A9) and (A11) to equation (A10) yields an expression for deformation incidence in terms of aerodynamic segment forces,  $\{f_T^A\}_1$ :

$$\{\theta^*\}_1 = [\tilde{C}_{\theta T}]_1 \{f_T^A\}_1 \quad (A12)$$

where

$$[\tilde{C}_{\theta T}]_1 \equiv [P_\theta] [\tilde{C}]_1 [P_T]^T$$

*Combined aerodynamic and structural equations-* In order to obtain a linear expression in the unspecified trim variables, the third term in equation (A6) representing the leading-edge correction effects is deleted from the aerodynamic representation. Substitution of equation (A7) into equation (A6) reduces equation (A6) to the following form:

$$\{f_T^A\}_1 = [T_{fT}] \{f_T^A\}_1 \quad (A13)$$

where the term  $\{f_T^A\}_1$  is defined by those terms in the right side of (A6) which post-multiply  $[T_{fT}]$  after leading-edge correction effects have been deleted. Furthermore,  $\{f_T^A\}_1$  is separated into two parts:

$$\{f_T^A\}_1 = [T_{TF}] \{F^A\}'_1 + \{f_T^A\}'_1 \quad (A14)$$

where

$$\{F^A\}'_1 = \bar{q}_1 [A_{F\theta}]_1 \{\theta^*\} \quad (A15)$$

and

$$\begin{aligned} \{P_T^A\}'_1 &= \bar{q}_1 [T_{TF}] [T_{FP}] \nabla q_c \nabla \left[ [A_{P\theta}] (\{\psi_c\}_1 + \{\psi_M\}_1) + \{C_p^V\}^{int} \right] \\ &+ \bar{q}_1 [TRANS_t] \nabla \bar{q}_t \nabla \left( \{C_p^S\}^{iso} + \nabla \Delta M \nabla \left\{ \frac{\partial C_p^S}{\partial M} \right\}^{iso} \right) \end{aligned} \quad (A16)$$

Explicit expression of  $\{f_T^A\}_1$  in terms of  $\{\theta^*\}$  can now be eliminated by substituting equations (A12) and (A15) into equation (A14), that is,

$$\{f_T^A\}_1 = (\mathbf{I} - \bar{q}_1 [T_{TF}] [A_{F\theta}]_1 [\tilde{C}_{\theta T}]_1)^{-1} \{f_T^A\}'_1 \quad (A17)$$

In order to save the computational time in matrix operations, equation (A17) is reduced to the form:

$$\{f_T^A\}_1 = (\mathbf{I} + \bar{q}_1 [T_{TF}] [\tilde{D}]_1^{-1} [A_{F\theta}]_1 [\tilde{C}_{\theta T}]_1) \{f_T^A\}'_1 \quad (A18)$$

where the aeroelastic matrix is identified as:

$$[\tilde{D}]_1^{-1} = \mathbf{I} - \bar{q}_1 [A_{F\theta}]_1 [\tilde{C}_{\theta T}]_1 [T_{TF}]$$

The term  $\{f_T^A\}'_1$  in equation (A18) can be identified as

$$\{f_T^A\}'_1 = \bar{q}_1 [T_{TF}] [A_{F\theta}]_1 (\{\psi_C\}_1 + \{\psi_M\}_1) + \{f_T^A\}^{int} + \{f_T^A\}^{iso} \quad (A19)$$

in which

$$\begin{aligned} \{f_T^A\}^{iso} &\equiv \bar{q}_1 [TRANS_t] \mathbf{I} \bar{q}_t \mathbf{J} \left( \{C_p^S\}_1^{iso} + \mathbf{I} \Delta M \mathbf{J} \left\{ \frac{\partial C_p^S}{\partial M} \right\}_1^{iso} \right) \\ \{f_T^A\}^{int} &\equiv \bar{q}_1 [T_{TF}] [T_{FP}] \mathbf{I} q_c \mathbf{J} \{C_p^V\}^{int} \end{aligned}$$

The derivation of equation (A18) can be accomplished by using a matrix identity,

$$\bar{q}_1 [T_{TF}] [\tilde{D}]_1^{-1} [A_{F\theta}]_1 [\tilde{C}_{\theta T}] + \mathbf{I} \mathbf{J} \equiv ([I] - \bar{q}_1 [T_{TF}] [A_{F\theta}]_1 [\tilde{C}_{\theta T}]_1)^{-1}$$

*Aerodynamic derivatives for a flexible aircraft-* Combining equations (A4), (A5), (A13), (A18), and (A19) leads to a complete expression for the total aerodynamic forces in the Body Axis System:

$$\{F_B^A\}_1 = ([G_T] + \bar{q}_1 [G_\theta] [\tilde{C}_{\theta T}]_1) (\{f_T^A\}^{iso} + \{f_T^A\}^{int}) + \bar{q}_1 G_\theta (\{\psi_C\}_1 + \{\psi_M\}_1) \quad (A20)$$

where

$$\begin{aligned} [G_T] &= 2[S][\phi^*][T_{fT}] \\ [G_\theta] &= [G_T] [\tilde{D}]_1^{-1} [T_{TF}] [A_{F\theta}] \end{aligned} \quad (A21)$$

The longitudinal aerodynamic derivatives can now be obtained by equating equations (A2) and (A20):

$$\begin{bmatrix} F_{XB_0}^A \\ F_{ZB_0}^A \\ M_{TB_0}^A \end{bmatrix}_E = ([G_T] + \bar{q}_1 [G_\theta] [\tilde{C}_{\theta T}]) (\{f_T^A\}_1^{iso} + \{f_T^A\}_1^{int}) + \bar{q}_1 [G_\theta] \{\psi_c\}_1 \quad (A22)$$

where

$$\begin{aligned} \{f_T^A\}_1^{iso} &\equiv \bar{q}_1 [TRANS_t] \nabla I_t \nabla \{C_p^S\}_1^{iso} \\ \{f_T^A\}_1^{int} &\equiv \bar{q}_1 [T_{TF}] [T_{FP}] \nabla I_c \nabla \{C_p^V\}^{int} \end{aligned} \quad (A23)$$

$$\begin{bmatrix} F_{XB_\alpha}^A \\ F_{ZB_\alpha}^A \\ M_{YB_\alpha}^A \end{bmatrix}_E = \bar{q}_1 [G_\theta] \{\psi_\alpha\} \quad (A24)$$

$$\begin{bmatrix} F_{XB_Q}^A \\ F_{ZB_Q}^A \\ M_{YB_Q}^A \end{bmatrix}_E = \bar{q}_1 [G_\theta] \{\psi_Q\} \frac{1}{U_1} \quad (A25)$$

$$\begin{bmatrix} F_{XB_{\delta_e}}^A \\ F_{ZB_{\delta_e}}^A \\ M_{YB_{\delta_e}}^A \end{bmatrix}_E = \bar{q}_1 [G_\theta] \{\psi_{\delta_e}\} \quad (A26)$$

The subscript E refers to an elastic aircraft.

*Aerodynamic derivatives for a rigid aircraft-* The flexible aircraft aerodynamic derivatives expressed by equations (A22) to (A26) consist of two quantities — the rigid aircraft aerodynamic derivatives and an increment due to the static aeroelasticity. This is accomplished by decomposing the matrix

$[G_\theta]$  into rigid and aeroelastic increment components by using the identity of the aeroelastic matrix  $[\tilde{D}]^{-1}$ :

$$[\tilde{D}]_1^{-1} \equiv \mathbf{I} + \bar{q}_1 [T_{TF}] [\tilde{D}]_1^{-1} [A_{F\theta}]_1 [\tilde{C}_{\theta T}] \quad (A27)$$

For a rigid aircraft the flexibility matrix vanishes; that is,  $[\tilde{C}_{\theta T}] = 0$ , and therefore  $[\tilde{D}]_1^{-1} = \mathbf{I}$ .

The aeroelastic component of  $[\tilde{D}]_1^{-1}$  can, therefore, be expressed as  $[\Delta D^{-1}] = [\tilde{D}]_1^{-1} - \mathbf{I}$ . It follows that  $[G_\theta]$  of equation (A21) can also be separated into two components: one for rigid aircraft component  $[G_{\theta R}]$  and the other for aeroelastic increment component  $[G_{\theta E}]$ ; that is,

$$G_\theta = [G_{\theta R}] + [G_{\theta E}] \quad (A28)$$

where

$$[G_{\theta R}] \equiv [G_T] [T_{TF}] [A_{F\theta}]$$

$$[G_{\theta E}] \equiv [G_T] [\Delta D^{-1}] [T_{TF}] [A_{F\theta}]_1$$

For a rigid aircraft the elastic rotation term  $\{\theta^*\}$  vanishes in equation (A12), that is,  $[\tilde{C}_{\theta T}] = 0$ , and the aerodynamic forces become

$$\{F_B^A\}_1 = [G_T] (\{f_T^A\}_1^{iso} + \{f_T^A\}_1^{int}) + \bar{q}_1 [G_{\theta R}] (\{\psi_c\}_1 + \{\psi_M\}_1) \quad (A29)$$

The longitudinal aerodynamic derivatives can be obtained by equating equations (A2) and (A29):

$$\left. \begin{aligned} \begin{bmatrix} F_{XB}^A \\ F_{ZB}^A \\ M_{YB}^A \end{bmatrix}_0 &= [G_T] (\{f_T^A\}_1^{iso} + \{f_T^A\}_1^{int}) + \bar{q}_1 [G_{\theta R}] \{\psi_c\}_1 \\ \begin{bmatrix} F_{XB}^A \\ F_{ZB}^A \\ M_{YB}^A \end{bmatrix}_\alpha &= \bar{q}_1 [G_{\theta R}] \{\psi_\alpha\} \end{aligned} \right\}$$

(A30) continued on next page

$$\left[ \begin{array}{c} F_{XB}^A \\ F_{ZB}^A \\ M_{YB}^A \end{array} \right]_R = \bar{q}_1 [G_{\theta R}] \{\psi_Q\} \frac{1}{U}$$

$$\left[ \begin{array}{c} F_{XB}^A \\ F_{ZB}^A \\ M_{YB}^A \end{array} \right]_R = \bar{q}_1 [G_{\theta R}] \{\psi_{\delta_e}\}$$

(A30) concluded

*Aeroelastic increment to the aerodynamic derivatives-* Substitution from equation (A28) to equation (A22) separates the aerodynamic derivatives for a flexible aircraft into two parts: one for the rigid aircraft and the other for the aeroelastic increment; that is,

$$\left[ \begin{array}{c} F_{XB}^A \\ F_{ZB}^A \\ M_{YB}^A \end{array} \right]_\lambda = \left[ \begin{array}{c} F_{XB}^A \\ F_{ZB}^A \\ M_{YB}^A \end{array} \right]_R + \left[ \begin{array}{c} \Delta F_{XB}^A \\ \Delta F_{ZB}^A \\ \Delta M_{YB}^A \end{array} \right]_E, \quad (A31)$$

where the subscript  $\lambda$  takes 0,  $\alpha$ , Q, or  $\delta_e$ . The aeroelastic increment to the aerodynamic derivatives can be written as

$$\left[ \begin{array}{c} \Delta F_{XB}^A \\ \Delta F_{ZB}^A \\ \Delta M_{YB}^A \end{array} \right]_0 = \bar{q}_1 [G_\theta] [\tilde{C}_{\theta T}] (\{f_T^A\}_1^{iso} + \{f_T^A\}^{int}) + \bar{q}_1 [G_{\theta E}] \{\psi_c\}$$

$$\left[ \begin{array}{c} \Delta F_{XB}^A \\ \Delta F_{ZB}^A \\ \Delta M_{YB}^A \end{array} \right]_\alpha = \bar{q}_1 [G_{\theta E}] \{\psi_\alpha\}$$

(A32) continued on next page

$$\left. \begin{aligned} & \left[ \begin{array}{c} \Delta F_{XB}^A \\ \Delta F_{ZB}^A \\ \Delta M_{YB}^A \end{array} \right]_Q \\ & \equiv \bar{q}_1 [G_{\theta E}] \{ \psi_Q \} \frac{1}{U_1} \\ & \left[ \begin{array}{c} \Delta F_{XB}^A \\ \Delta F_{ZB}^A \\ \Delta M_{YB}^A \end{array} \right]_{\delta_e} \\ & \equiv \bar{q}_1 [G_{\theta E}] \{ \psi_{\delta_e} \} \end{aligned} \right\}$$

(A32) concluded

#### Implementation of Experimental Aerodynamic Force Into the Linear Theory

*Force correction-* The approach of implementing the experimental aerodynamic forces into the linear theory solution of the FLEXSTAB is based on the theoretical foundation that aerodynamic derivatives are composed of rigid components and elastic component increments.

The effect of the experimental aerodynamic force incorporation is on the rigid term only in equation (A31). The elastic increment term on the right side of equation (A31) is calculated based on the linear theories represented by equation (A32).

In this approach, the rigid component of the trim solution is forced to represent the wind-tunnel data accurately, and to allow the experimental data to represent global effects of the nonlinear flow. The linear theory is to use the rigid wind tunnel results as a baseline to estimate the elastic effects of the actual airframe configuration.

The aerodynamic force data are supplied to the FLEXSTAB system in terms of  $C_L$ ,  $C_D$ , and  $C_m$  which are tabulated for various angles of attack for constant elevon deflections. Since the data for  $C_L$ ,  $C_D$ , and  $C_m$  are measured in reference to a Stability Axis System, the data are transformed to a Body Axis System in order to be compatible with equation (A1). The equation of transformation can be written as follows:

$$\left[ \begin{array}{c} F_{XB}^A \\ F_{ZB}^A \\ M_{YB}^A \end{array} \right]_R = [SD^S] \left[ \begin{array}{c} C_L \\ C_D \\ C_m \end{array} \right]_R \quad (A33)$$

where  $[SD^S]$  is a transformation matrix defined in chapter 5 of reference 1.

## Implementation of Experimental Pressure Into the Linear Theory - Pressure Correction

The effect of the pressure correction is twofold — one on the rigid aerodynamic derivatives and the other on the aeroelastic increment to the aerodynamic derivatives. These effects can be demonstrated as follows. The body face expressed in the local coordinate system can be written in the form:

$$\begin{aligned} \{f_T^A\}_1 &= \bar{q}_1 [T_{TF}] [\tilde{D}]_1^{-1} [A_{F\theta}] (\{\psi_c\} + \{\psi_M\}) + \bar{q}_1 [T_{TF}] [\tilde{D}]_1^{-1} [T_{TP}] \nabla q_c \nabla [C_p^V]^{int} \\ &+ \bar{q}_1 [T_{TF}] [\tilde{D}]_1^{-1} [A_{F\theta}] [\tilde{C}_{\theta T}] \{f_T^A\}_1^{iso} + \{f_T^A\}_1^{iso} \end{aligned} \quad (A34)$$

In FLEXSTAB, the last term in equation (A34) is omitted so that it can be expressed as

$$\{f_T^A\}_1 = [T_{TF}] \{F^A\}_1$$

where

$$\{F^A\}_1 = [\tilde{D}]_1^{-1} \left[ [A_{F\theta}] \left( [\{\psi_c\} + \{\psi_M\}] + \bar{q}_1 [\tilde{C}_{\theta T}] \{f_T^A\}_1^{iso} \right) + \bar{q}_1 [T_{FP}] \nabla q_c \nabla [C_p^V]^{int} \right] \quad (A35)$$

Equation (A35) transforms the normal force components at the aerodynamic centroids  $\{F^A\}_1$  expressed in the Reference Axis System to components on the local axis system  $\{f_T^A\}_1$ . The normal pressure coefficients are defined in terms of  $\{F^A\}_1$  by

$$\{\Delta C_p\} = \frac{1}{\bar{q}_1} [T_{\Delta p}] \{F^A\}_1$$

where

$$[T_{\Delta p}] = \text{Diag} \left[ \frac{1}{S_{ZM_1}}, \frac{1}{S_{ZM_2}}, \dots, \frac{1}{S_{ZM_n}}, \frac{1}{S_{ZW_1}}, \frac{1}{S_{ZW_2}}, \dots, \frac{1}{S_{ZW_m}} \right]$$

$S_{ZM_n}$  and  $S_{ZW_m}$  denote area for  $n$ th slender-body segment and  $m$ th thin-body panel, respectively. Specifically, for a slender body on the plane of symmetry, the area  $S_{ZM_i}$  is given as

$$S_{ZM_i} = \pi A_i$$

where  $A_i$  is the area projection of  $i$  segment on  $x-y$  plane as shown in figure 1. The area of the wing panel,  $S_{ZW_m}$ , is the associate panel area on the wing mean surface.

FLEXSTAB allows the user to provide linear corrective inputs to modify the pressure computed using the linear theory. Assume that at the  $i$ th aerodynamic control point, the plot of  $\Delta C_{p_i}$  versus angle of attack is as shown in figure 15. Suppose for FLEXSTAB,

$$\Delta C_{p_i}^{\mathcal{F}} = \Delta C_{p_{i_0}}^{\mathcal{F}} + \Delta C_{p_{i_\alpha}}^{\mathcal{F}} \alpha \quad (\text{A36})$$

while from experiment

$$\Delta C_{p_i}^{\text{WT}} = \Delta C_{p_{i_0}}^{\text{WT}} + \Delta C_{p_{i_\alpha}}^{\text{WT}} \alpha \quad (\text{A37})$$

FLEXSTAB corrects equation (A36) by adding the term

$$\Delta C_{p_{i_0}} + \Delta C_{p_{i_\alpha}} \alpha \quad (\text{A38})$$

where

$$\Delta C_{p_{i_0}} = \Delta C_{p_{i_0}}^{\text{WT}} - \Delta C_{p_{i_0}}^{\mathcal{F}} \quad (\text{A38})$$

$$\Delta C_{p_{i_\alpha}} = \Delta C_{p_{i_\alpha}}^{\text{WT}} - \Delta C_{p_{i_\alpha}}^{\mathcal{F}}$$

The nonlinear experimental data are, in practice, represented by a linear approximation. The data are added on equation (A35), and the corrected pressure and aerodynamic force can be expressed as:

$$\{\Delta C_p\}_c = \frac{1}{\bar{q}_1} [T_{\Delta p}] \{F^A\}_1 + \{\Delta C_{p_0}\} + \{\Delta C_{p_\alpha}\} \alpha \quad (\text{A39})$$

$$\begin{aligned} \{F^A\}_{1_c} &= \bar{q}_1 [T_{\Delta p}]^{-1} \{\Delta C_p\} \\ &= \{F^A\}_1 + \bar{q}_1 [T_{\Delta p}]^{-1} \left( \{\Delta C_{p_0}\} + \{\Delta C_{p_\alpha}\} \alpha \right) \end{aligned} \quad (\text{A40})$$

FLEXSTAB transforms normal pressure to normal forces using the matrix  $[T_{TF}] = [T_{\Delta p}]^{-1}$ . The corrected form for equation (A19) becomes

$$\begin{aligned} \{f_T^A\}_{1_c}' &= \bar{q}_1 [T_{TF}] [A_{F\theta}] (\{\psi_c\}_1 + \{\psi_M\}_1) + \{f_T^A\}^{\text{int}} + \{f_T^A\}^{\text{iso}} \\ &\quad + \bar{q}_1 [T_{TF}] [T_{FP}] (\{\Delta C_{p_0}\} + \{\Delta C_{p_\alpha}\} \alpha) \end{aligned} \quad (\text{A41})$$

and the corrected body force corresponding to (A20) becomes

$$\{F_B^A\}_{1c} = ([G_T] + \bar{q}_1 [G_\theta] [\tilde{C}_{\theta T}]_1) \{f_T^A\}'_{1c} \quad (A42)$$

The corrected aerodynamic derivatives can be derived by comparing the corresponding terms in equations (A42) and (A20). In elastic case,

$$\begin{bmatrix} F_{XB_0c}^A \\ F_{ZB_0c}^A \\ M_{YB_0c}^A \end{bmatrix}_E = ([G_T] + \bar{q}_1 [G_\theta] [\tilde{C}_{\theta T}]_1) (\{f_T^A\}_{1c}^{iso} + \{f\}_{1c}^{int}) + \bar{q}_1 [G_\theta] \{\psi_c\}_1 + \bar{q}_1 [G_T] [T_{TF}] [\tilde{D}]^{-1} [T_{FP}] \{\Delta C_{P_0}\} \quad (A43)$$

$$\begin{bmatrix} F_{XB_\alpha c}^A \\ F_{ZB_\alpha c}^A \\ M_{YB_\alpha c}^A \end{bmatrix}_E = \bar{q}_1 [G_\theta] \{\psi_\alpha\} + \bar{q}_1 [G_T] [T_{TF}] [\tilde{D}]^{-1} [T_{FP}] \{\Delta C_{P_\alpha}\} \quad (A44)$$

In the rigid case:

$$\begin{bmatrix} F_{XB_0c}^A \\ F_{ZB_0c}^A \\ F_{YB_0c}^A \end{bmatrix}_R = [G_T] (\{f_T^A\}_{1c}^{iso} + \{f_T^A\}_{1c}^{int}) + \bar{q}_1 [G_{\theta R}] \{\psi_c\}_1 + \bar{q}_1 [G_T] [T_{TF}] [T_{FP}] \{\Delta C_{P_0}\} \quad (A45)$$

$$\begin{bmatrix} F_{XB_\alpha c}^A \\ F_{ZB_\alpha c}^A \\ M_{YB_\alpha c}^A \end{bmatrix}_R = \bar{q}_1 [G_{\theta R}] \{\psi_\alpha\} + \bar{q}_1 [G_T] [T_{TF}] [T_{FP}] \{\Delta C_{P_\alpha}\} \quad (A46)$$

Equations (A43) to (A46) gives the corrected aeroelastic increment in the following form:

$$\begin{bmatrix} \Delta F_{XB_0}^A \\ \Delta F_{ZB_0}^A \\ \Delta M_{YB_0}^A \end{bmatrix}_E = \bar{q}_1 [G_\theta] [\tilde{C}_{\theta T}] (\{f_T^A\}_1^{iso} + \{f_T^A\}^{int}) + \bar{q}_1 [G_{\theta E}] \{\psi_c\} + \bar{q}_1 [G_T] [T_{TF}] [\Delta \tilde{D}^{-1}] [T_{FP}] \{\Delta C_{p_\alpha}\} \quad (A47)$$

$$\begin{bmatrix} \Delta F_{XB_\alpha}^A \\ \Delta F_{ZB_\alpha}^A \\ \Delta M_{YB_\alpha}^A \end{bmatrix}_E = \bar{q}_1 [G_{\theta E}] \{\psi_\alpha\} + q_1 [G_T] [T_{TF}] [\Delta \tilde{D}^{-1}] [T_{FP}] \{\Delta C_{p_\alpha}\} \quad (A48)$$

The effect of pressure on the aerodynamic derivatives is indicated by the last term in each of the above equations, (A43) to (A48). Note that all other derivatives are unaffected.

#### Implementation of Experimental Force and Pressure into the Linear Theory - Force and Pressure Correction Method

As the experimental force and pressure are implemented into FLEXSTAB, the supplied force data are used only in the rigid part of the computation by using equation (A33); the pressure data are used only in the computation of the aeroelastic increments by using equations (A47) and (A48). The global and local effects are thus achieved by implementing force and pressure data, respectively.

## REFERENCES

1. Dusto, A. R.; Brune, G. W.; Dornfeld, G. M.; Mercer, J. E.; Pilet, S. C.; Rubbert, P. E.; Schwanz, R. E.; Smutny, P.; Tinoco, E. N.; and Weber, J. A.: A Method for Predicting the Stability Characteristics of an Elastic Airplane. NASA CR-114712, October 1974, Boeing Commercial Airplane Company, Seattle, Washington.
2. Dornfeld, G. M.; Bhatia, K. G.; Maier, R. E.; Snow, R. N.; and Van Rossum, D. A.: A Method for Predicting the Stability Characteristics of an Elastic Airplane. Vol. IV-FLEXSTAB 1.02.00, Demonstration Cases and Results, November 1974.
3. Tinoco, Edward N: An Aeroelastic Analysis of the YF-12A Airplane Using the FLEXSTAB System (U). Paper No. 12, NASA TM X-3061, May 1974, (Confidential).
4. Aerodynamic Design Substantiation Report. Vol. 4, Orbiter Rotary Derivatives SD74-SH-0206-4G, prepared by Flight Dynamics Aerodynamics Space Division, Rockwell International, August 1974, Contract No. NAS9-14000.
5. Aerodynamic Design Data Book, Vol. I, Orbiter Vehicles. Prepared by Aero Sciences, Space Division, Rockwell International, SD72-SH-0060-1E, July 1973, Contract No. NAS9-14000.

TABLE 1.- CALCULATED AND EXPERIMENTAL AERODYNAMIC COEFFICIENTS FOR A RIGID ORBITER

Method	$C_{L_0}$	$C_{D_0}$	$C_{m_0}$
1	-0.17	0.001	0.1
2 and 4	-.08	.08	.06
3	-.09	.003	.004
Experiment	-.08	.08	.06

(1/deg)

TABLE 2.- STABILITY COEFFICIENTS FOR A RIGID-ORBITER CONFIGURATION ( $M = 0.9$ , 1.0 g)

	$C_{L_\alpha}$	$C_{D_\alpha}$	$C_{m_\alpha}$
Method 1	0.04	0.01	-0.001
Methods 2, 4 and experiment	.17	.02	-.004

(1/deg)

	$C_{L_\delta}$	$C_{D_\delta}$	$C_{m_\delta}$
Method 1	0.029	0.005	-0.015
Methods 2, 4, and experiment	.007	.004	-.009

(1/deg)

	$C_{L_{\hat{Q}}}$	$C_{D_{\hat{Q}}}$	$C_{m_{\hat{Q}}}$
Method 1	3.90	0.73	-1.99
Methods 2 and 4	3.90	.68	-1.99

(1/rad)

TABLE 3.- AERODYNAMIC DERIVATIVES FROM METHODS 2, 3, AND 4

	$C_{L_0}$	$C_{D_0}$	$C_{m_0}$
Method 3	-0.09	0.003	0.004
Methods 2, 4, and experiment	-.08	.08	.06

(1/deg)

	$C_{L_\alpha}$	$C_{D_\alpha}$	$C_{m_\alpha}$
Method 3	0.05	0.02	-0.002
Methods 2, 4, and experiment	.17	.02	-.004

(1/deg)

	$C_{L_{\hat{Q}}}$	$C_{D_{\hat{Q}}}$	$C_{m_{\hat{Q}}}$
Method 3	3.89	0.77	-0.199
Methods 2, 4, and experiment	3.90	.68	-.199

(1/rad)

	$C_{L_\delta}$	$C_{D_\delta}$	$C_{m_\delta}$
Method 3	0.029	0.029	-0.015
Methods 2, 4, and experiment	.007	.004	-.009

(1/deg)

TABLE 4.- AERODYNAMIC FORCES AND MOMENTS FOR THE RIGID  
AND FLEXIBLE ORBITER AT TRIM CONDITION

	1.0 g		2.5 g		
	Rigid	Elastic	Rigid	Elastic	
$\alpha$	9.5	9.5	19.7	19.7	
$\theta$	-11.0	-11.1	-47.8	-50.4	
$\delta$	7.4	7.6	12.5	13.7	(deg)
$C_{L_0}$	-.080	-.067	-.080	-.067	
$C_{D_0}$	.080	.080	.080	.080	
$C_{m_0}$	.060	.054	.060	.054	
$C_{L_\alpha}$	.17	.17	.012	.010	
$C_{D_\alpha}$	.02	.02	.018	.017	
$C_{m_\alpha}$	-.004	.004	.019	.020	(1/deg)
$C_{L_{\hat{Q}}}$	3.90	3.80	3.72	3.65	
$C_{L_{\hat{Q}}}$	.68	.66	1.36	1.33	
$C_{m_{\hat{Q}}}$	-1.99	-1.94	-1.99	-1.94	(1/rad)
$C_{L_\delta}$	.007	.005	.010	.008	
$C_{D_\delta}$	.004	.004	.007	.006	
$C_{m_\delta}$	-.009	-.008	-.007	-.006	(1/deg)

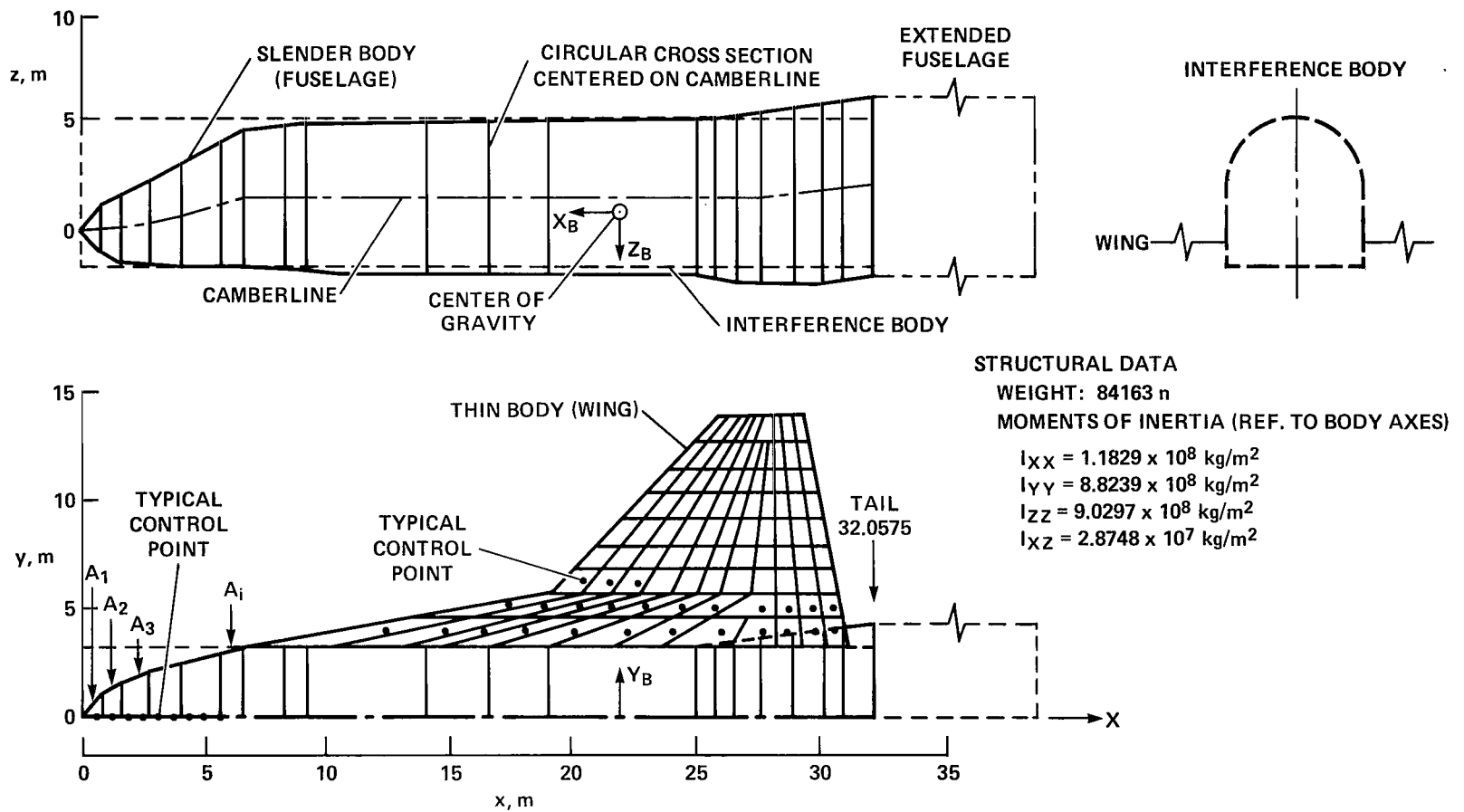


Figure 1.- Orbiter geometry and structural data.

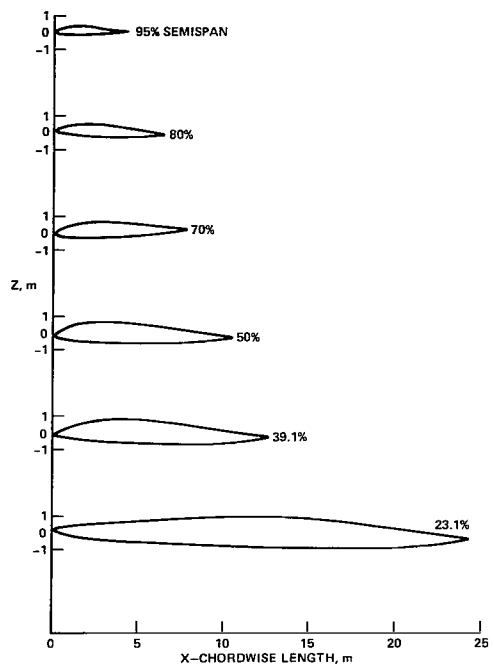


Figure 2.- Orbiter wing profile.

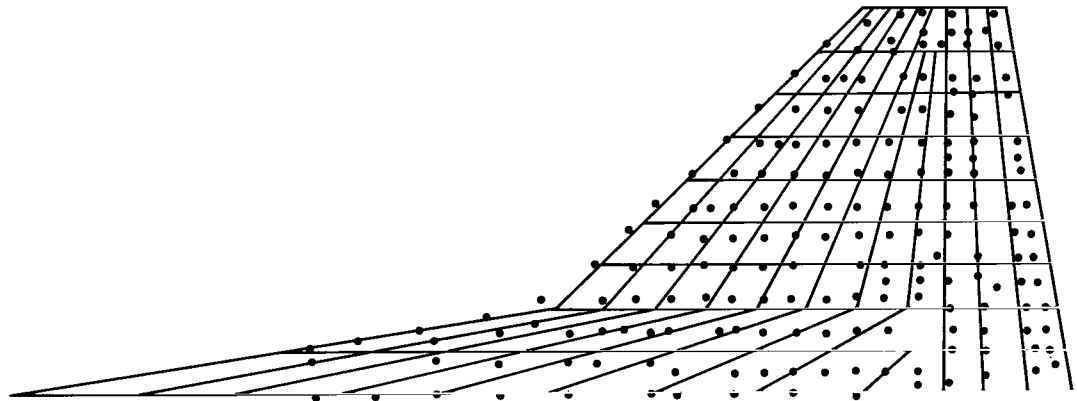
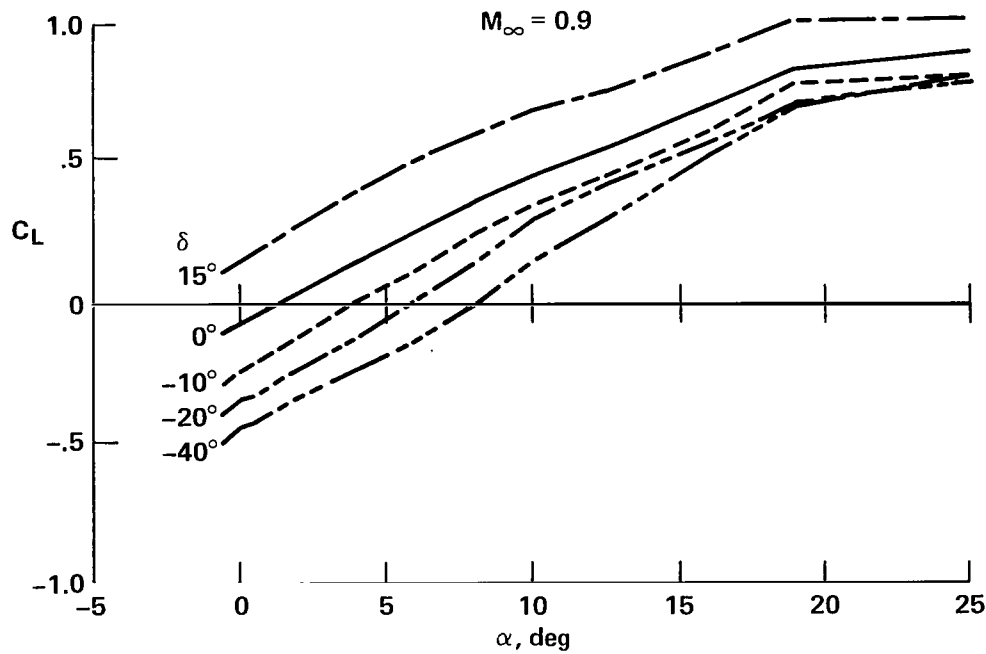
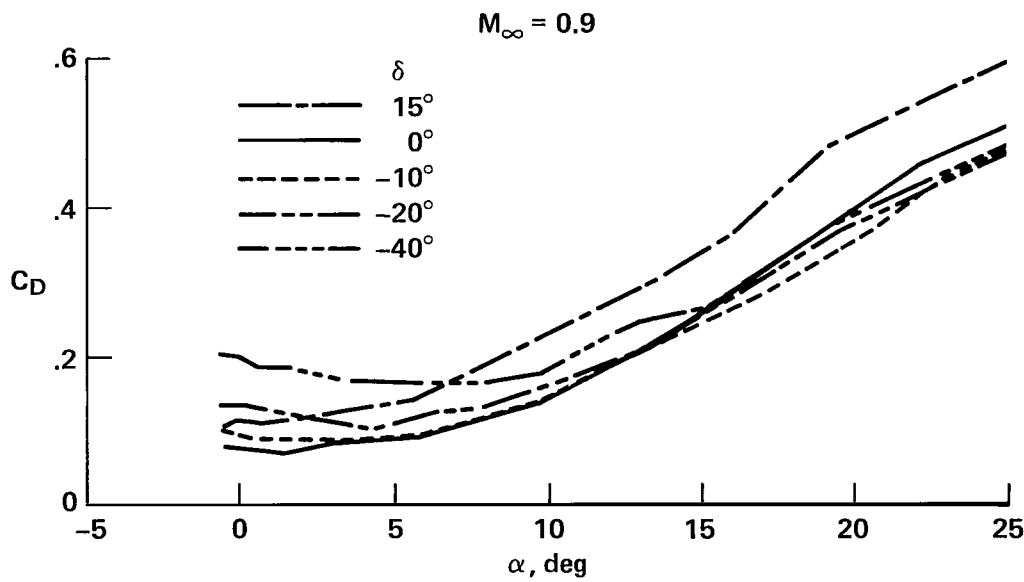


Figure 3.- Overlay of aerodynamic panels and structural node points.

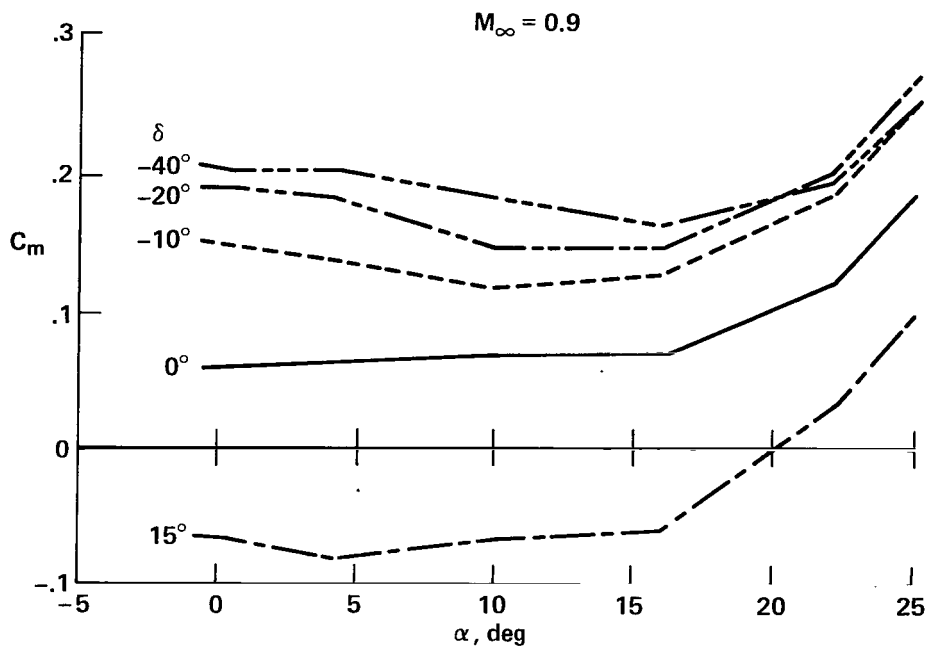


(a) Lift coefficient.



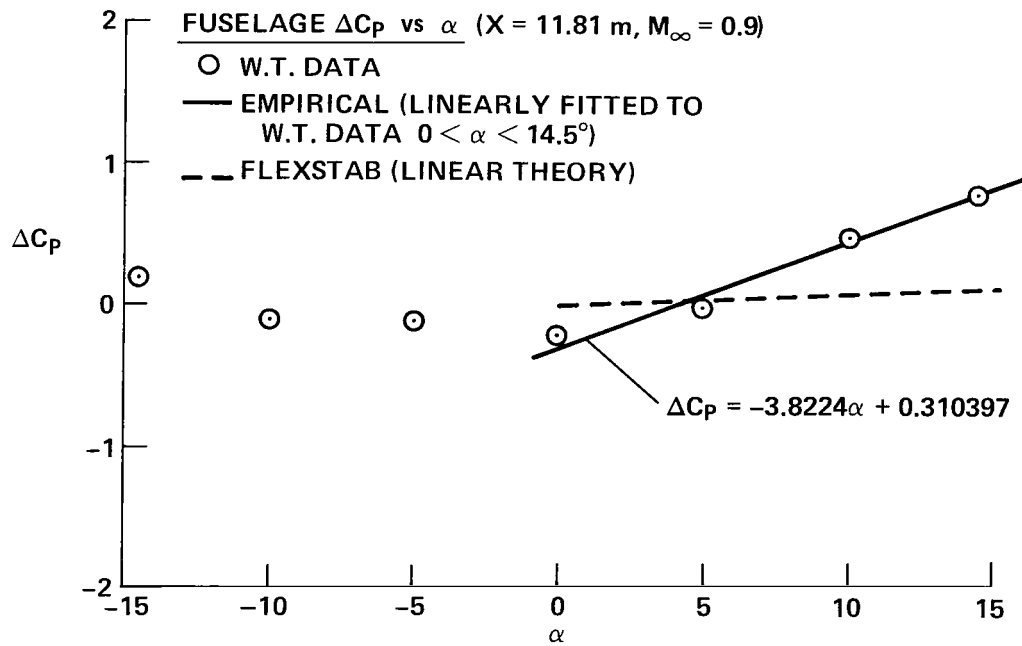
(b) Drag coefficient.

Figure 4.- Experimental aerodynamic forces and moments.



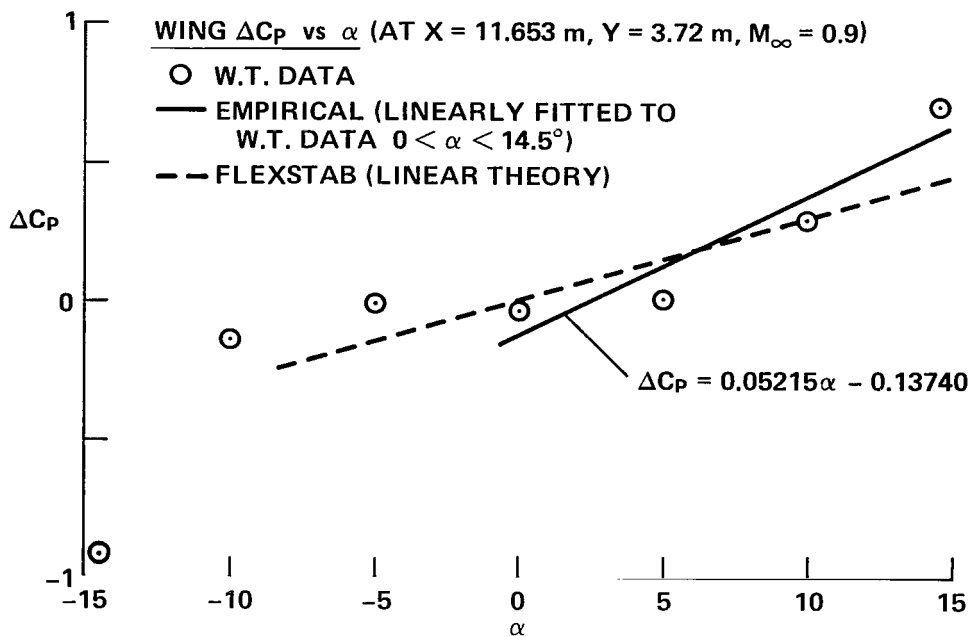
(c) Pitch-moment coefficient.

Figure 4.- Concluded.



(a) Fuselage pressure.

Figure 5.- Experimental lifting pressures representation.



(b) Wing pressure.

Figure 5.- Concluded.

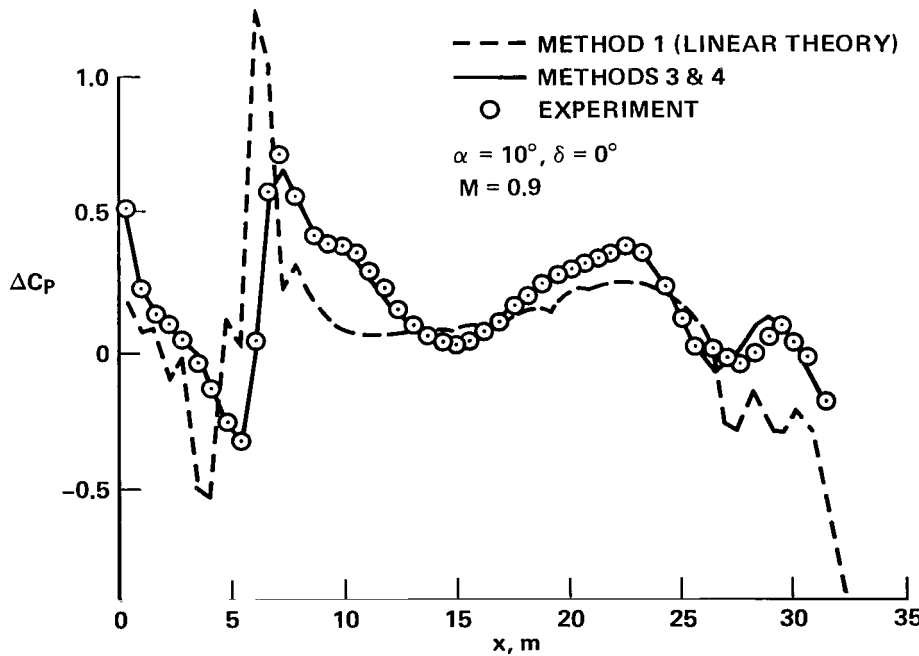
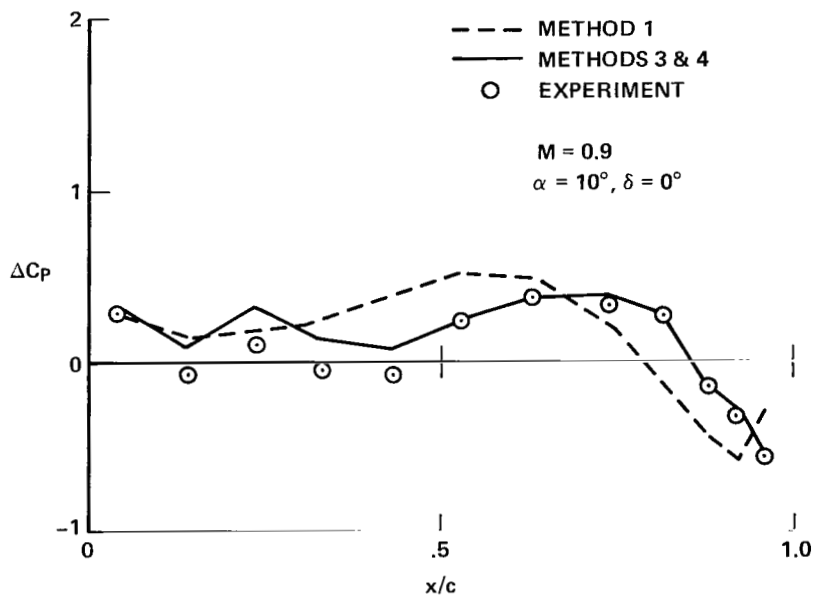
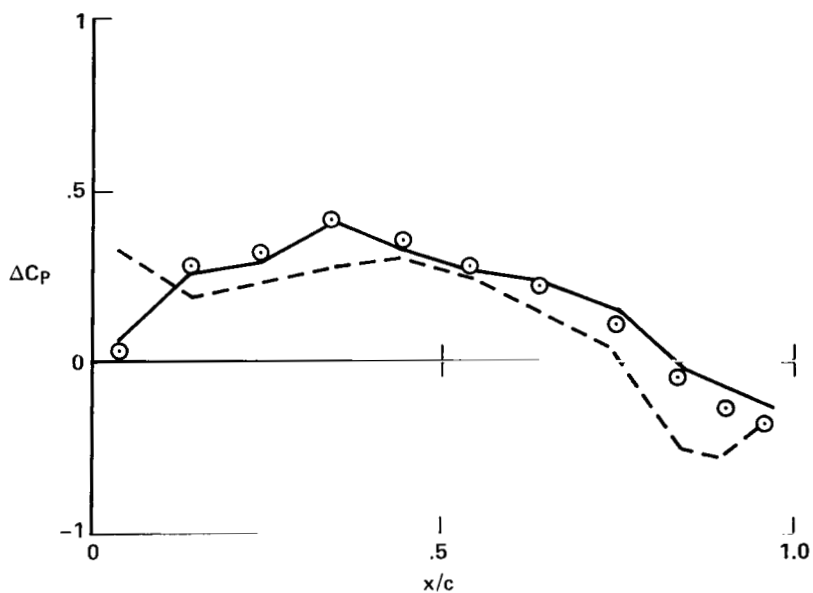


Figure 6.- Lifting pressures on fuselage (Methods 1, 3, 4, and experiment).

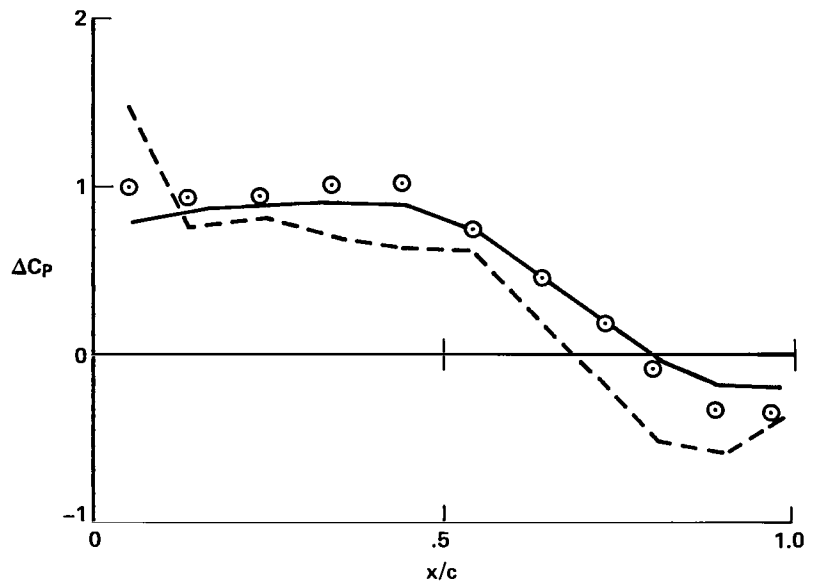


(a) 27.1% semispan.

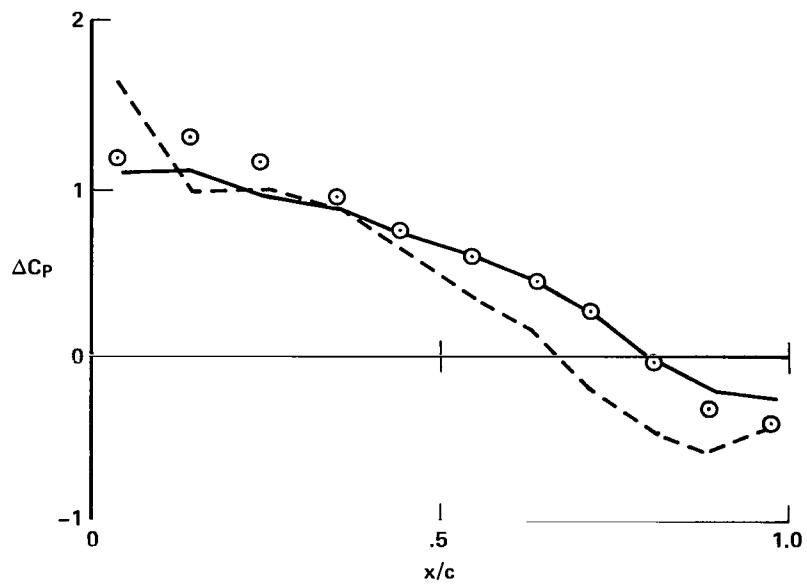


(b) 35.4% semispan.

Figure 7.- Chordwise lifting-pressure distribution (Methods 1, 3, 4, and experiment).

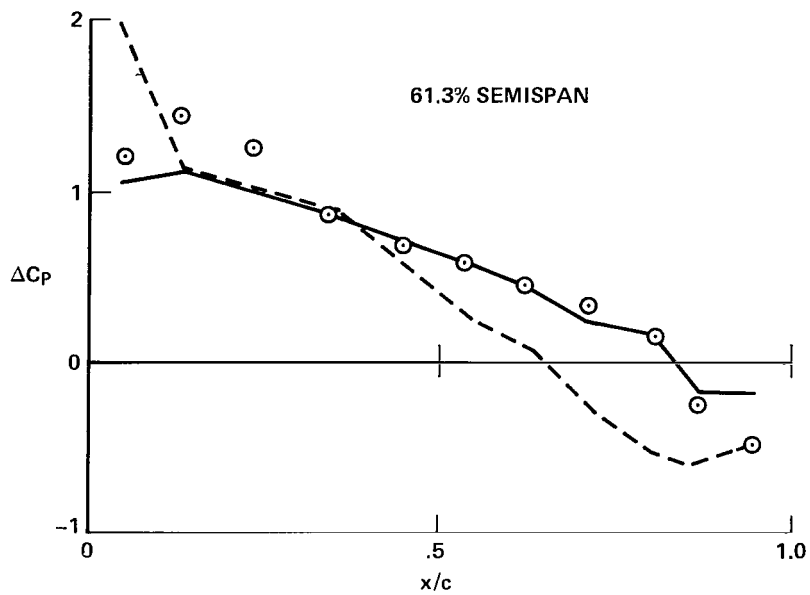


(c) 44.2% semispan.

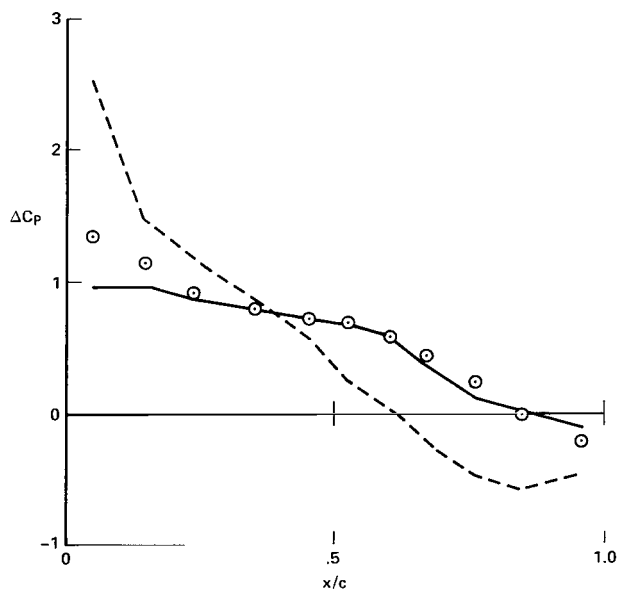


(d) 52.7% semispan.

Figure 7.- Continued.

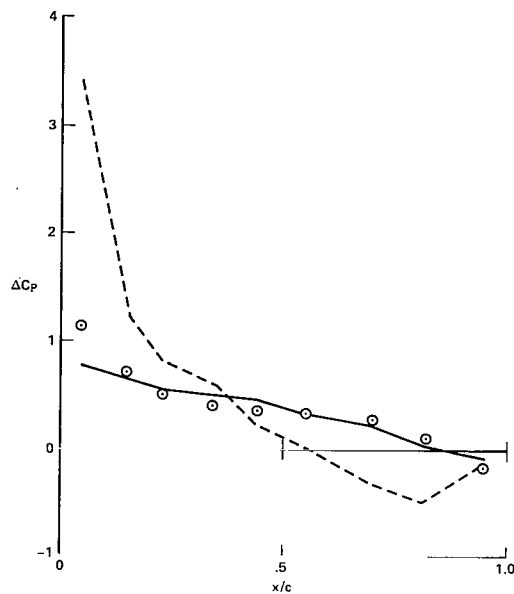


(e) 61.3% semispan.



(f) 78.3% semispan.

Figure 7.- Continued.



(g) 95.4% semispan.

Figure 7.- Concluded.

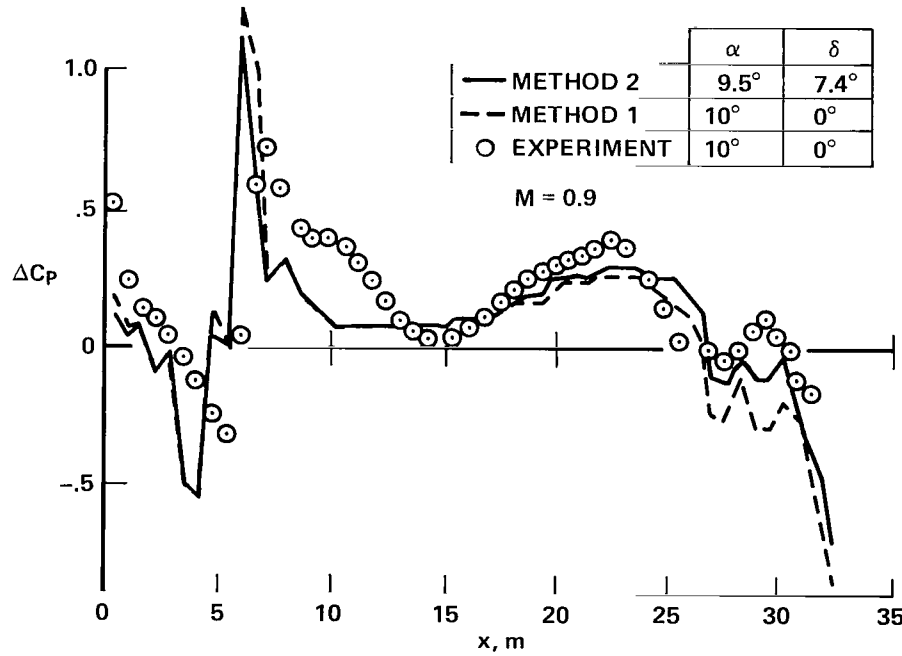
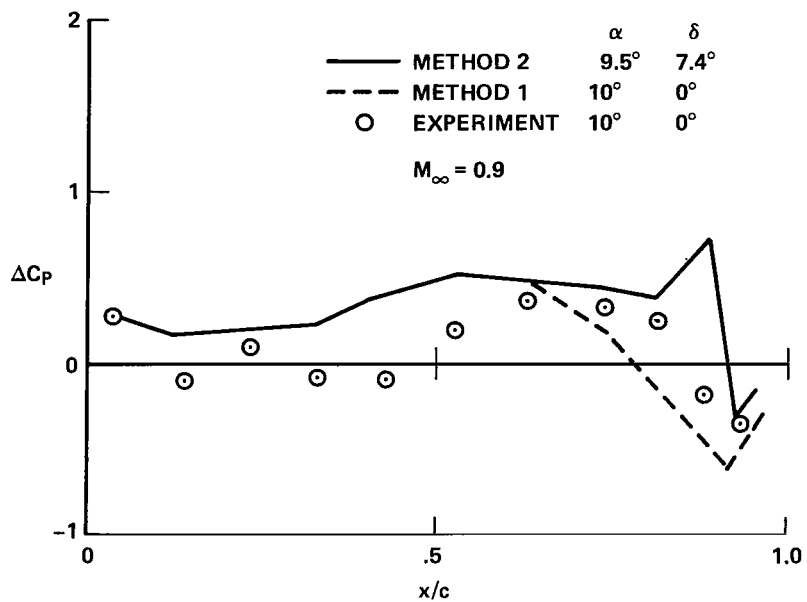
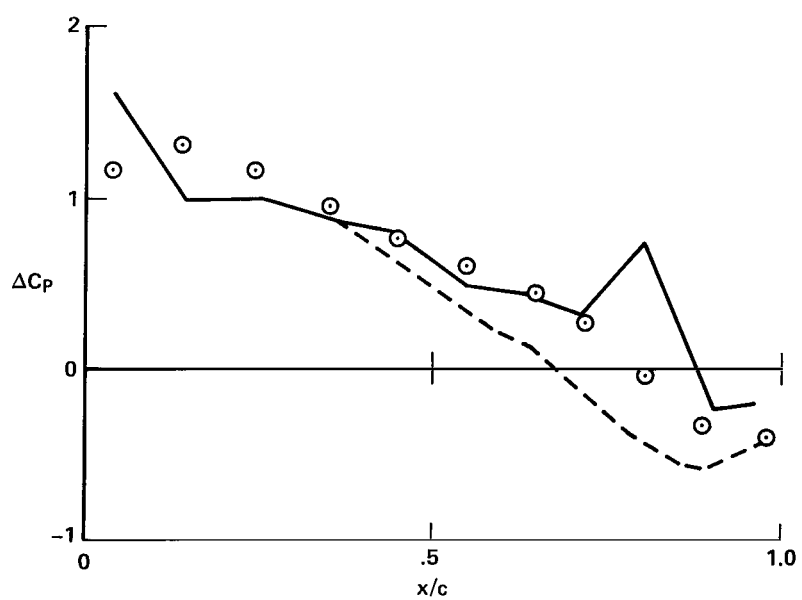


Figure 8.- Lifting pressures on fuselage (Methods 1, 2, and experiment).

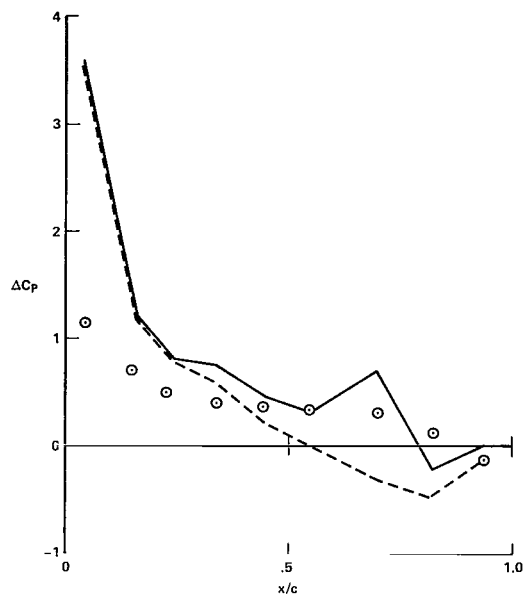


(a) 27.1% semispan.



(b) 52.7% semispan.

Figure 9.- Lifting pressures on wing (Methods 1, 2, and experiment).



(c) 95.4% semispan.

Figure 9.- Concluded.

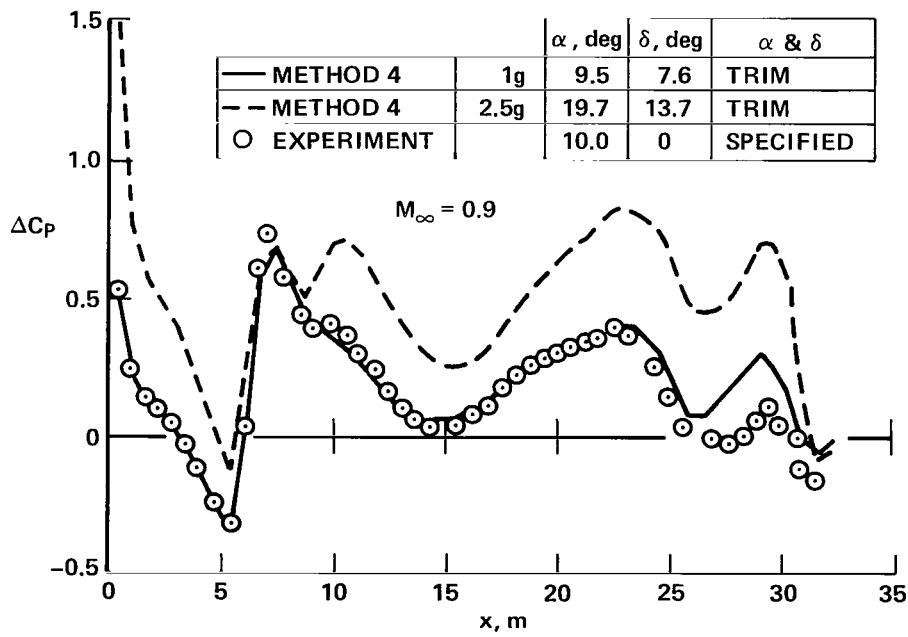
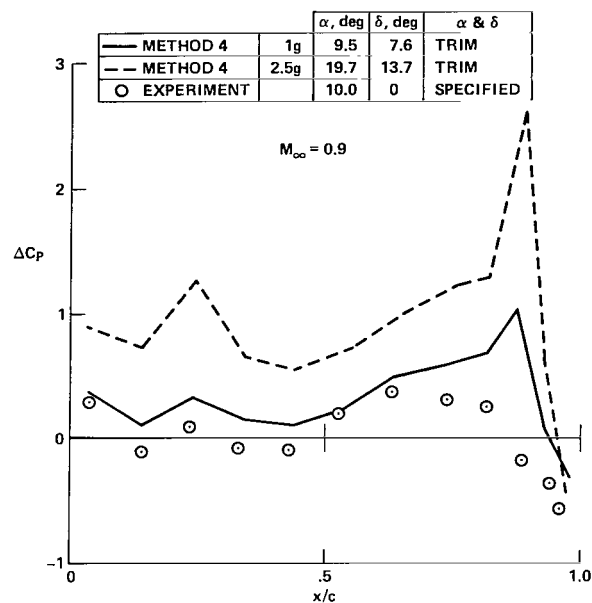
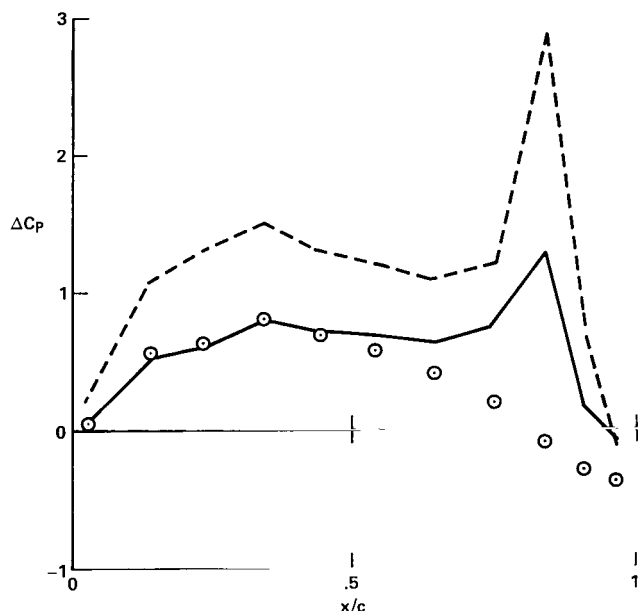


Figure 10.- Estimated lifting pressures on fuselage at 1-g and 2.5-g flight conditions.

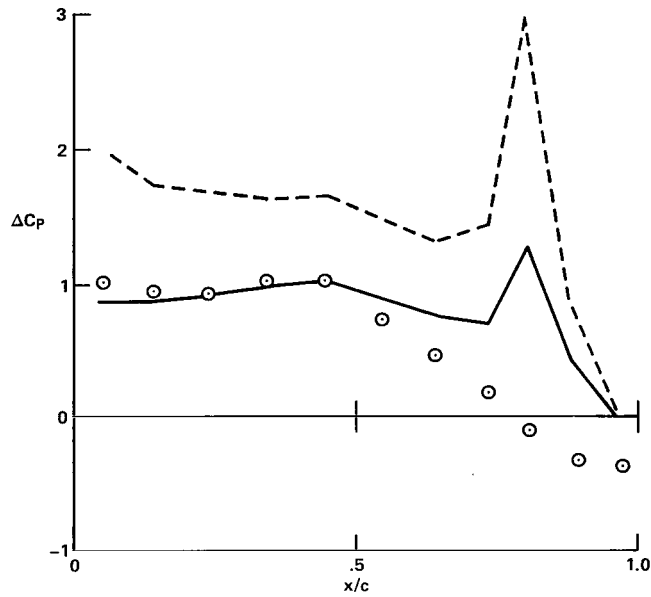


(a) 27.1% semispan.

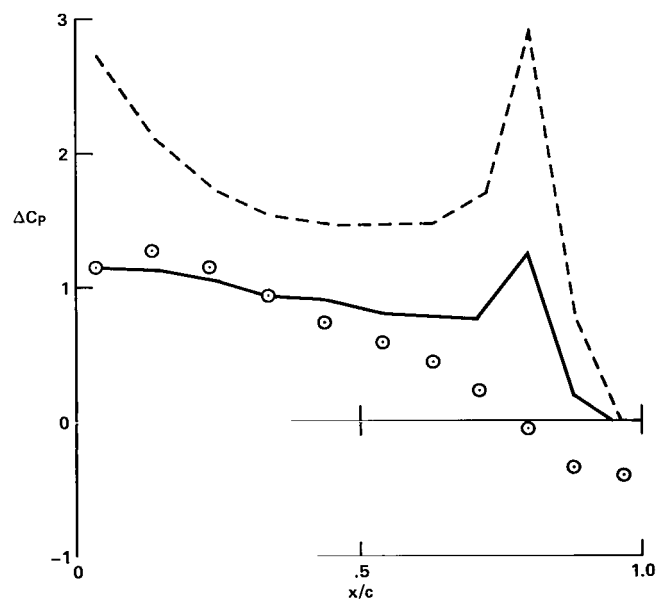


(b) 35.44% semispan.

Figure 11.- Estimated lifting pressures on wing at 1-g and 2.5-g flight conditions.

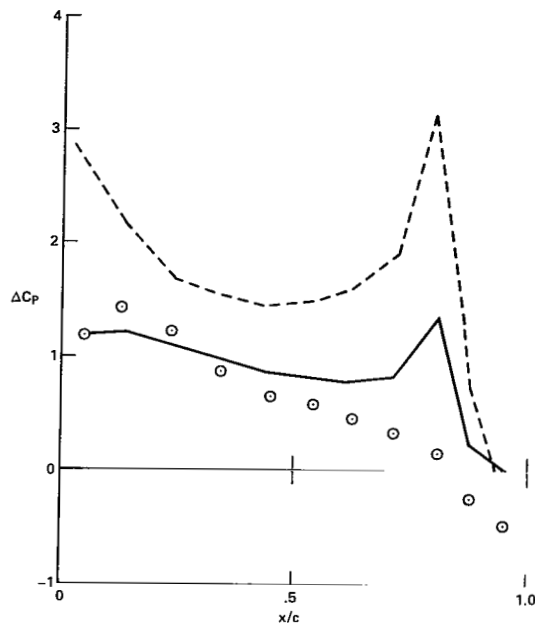


(c) 44.20% semispan.

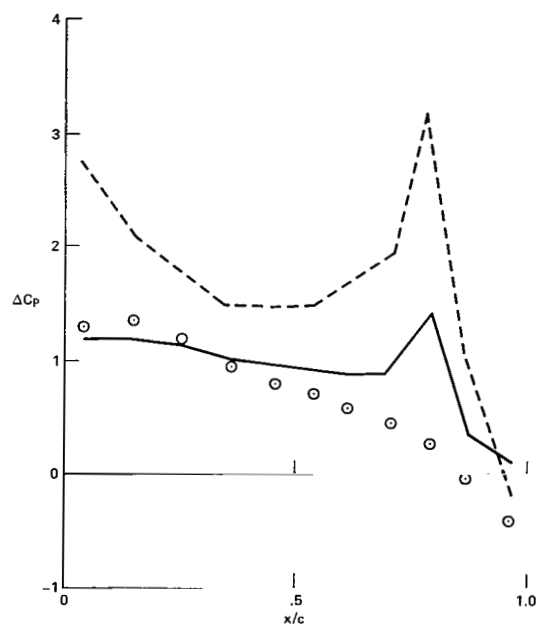


(d) 52.74% semispan.

Figure 11.- Continued.

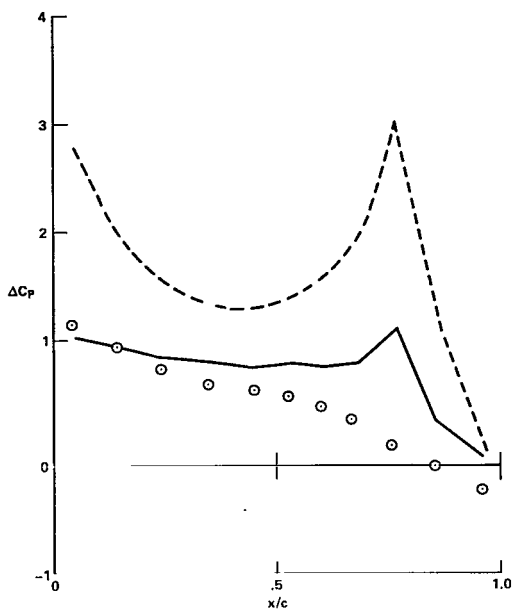


(e) 61.28% semispan.

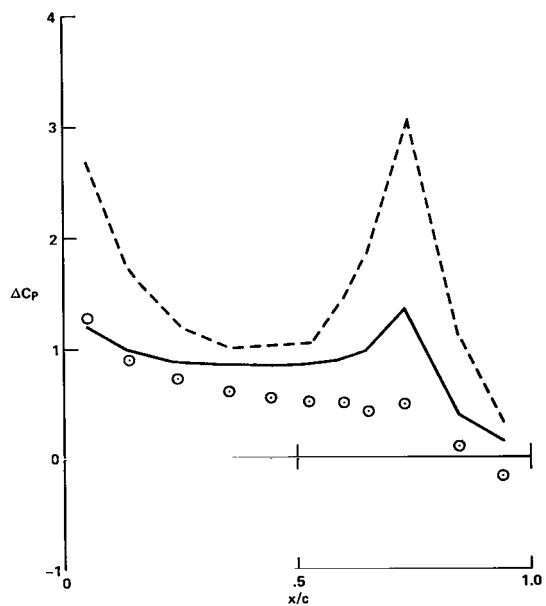


(f) 69.82% semispan.

Figure 11.- Continued.

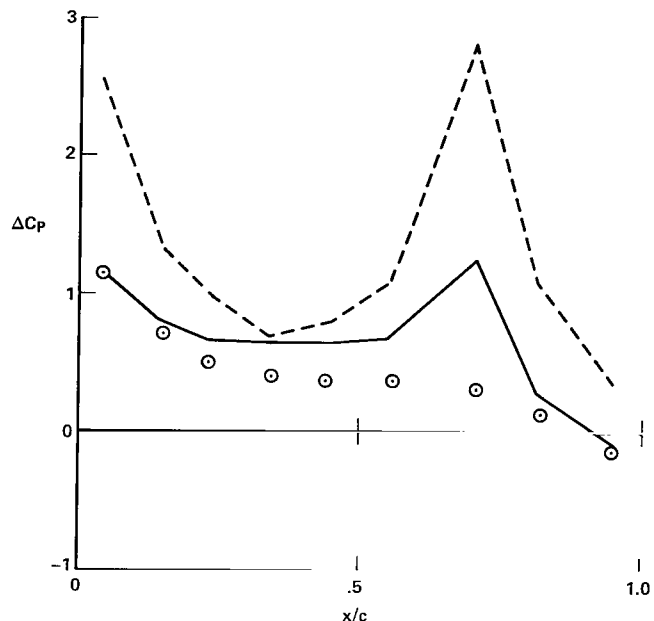


(g) 78.36% semispan.



(h) 86.90% semispan.

Figure 11.- Continued.



(i) 95.44% semispan.

Figure 11.- Concluded.

#### TRIM CONDITION

METHOD 4	$\alpha$ , deg	$\delta$ , deg	
	1g	9.5	7.6
	2.5g	19.7	13.7

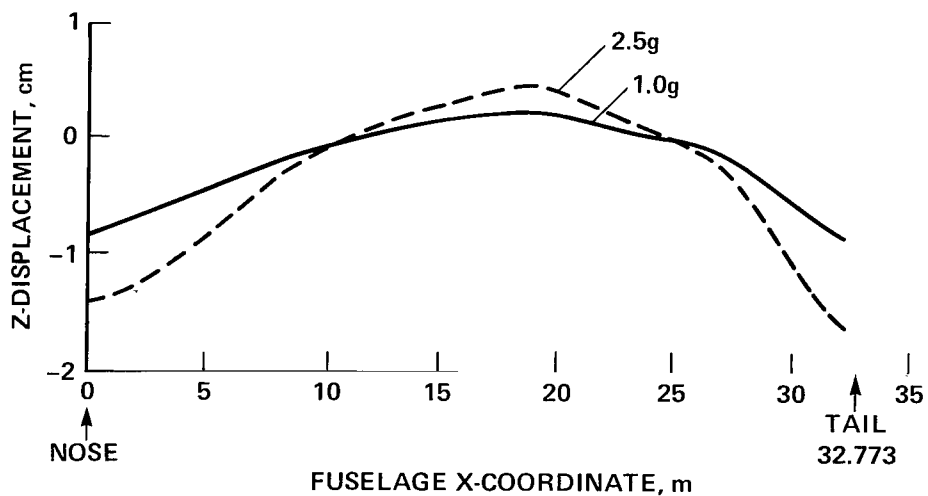
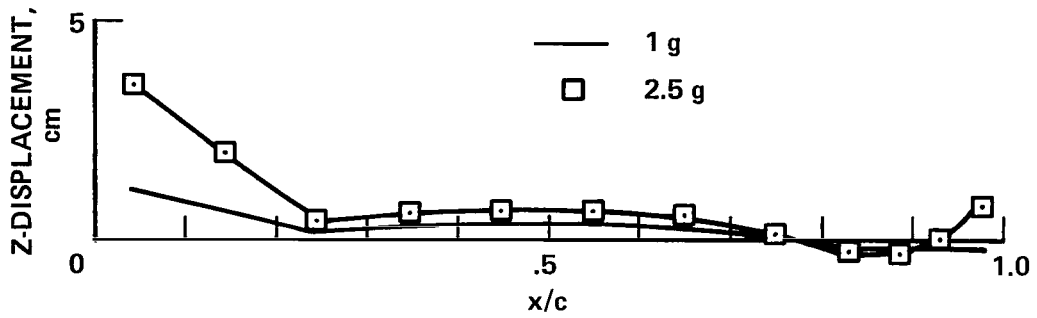
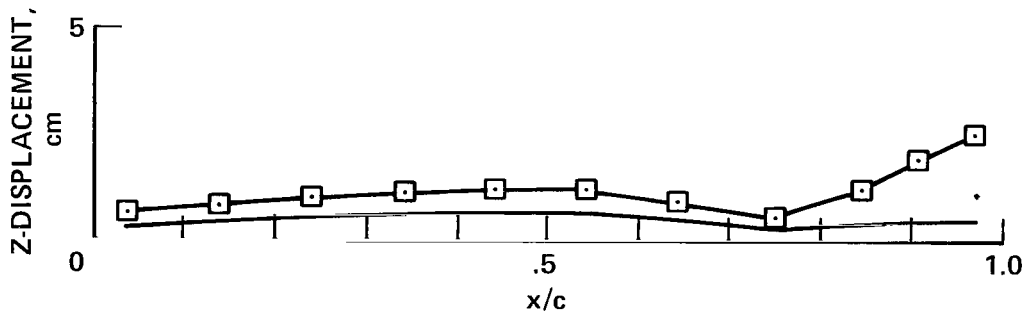


Figure 12.- Orbiter fuselage deformation.

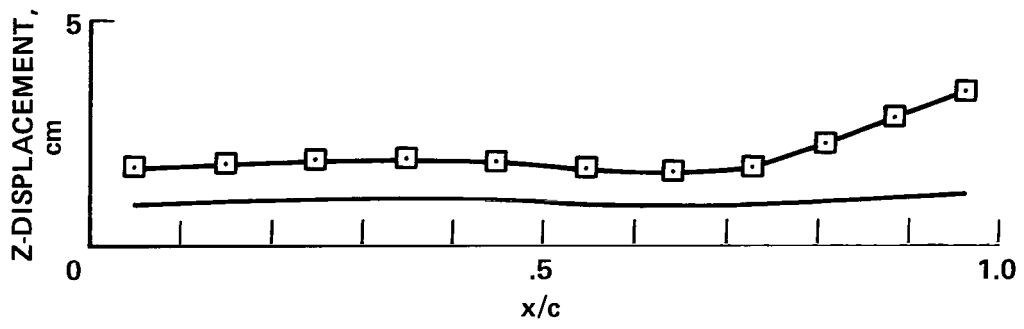


(a) 27% semispan.

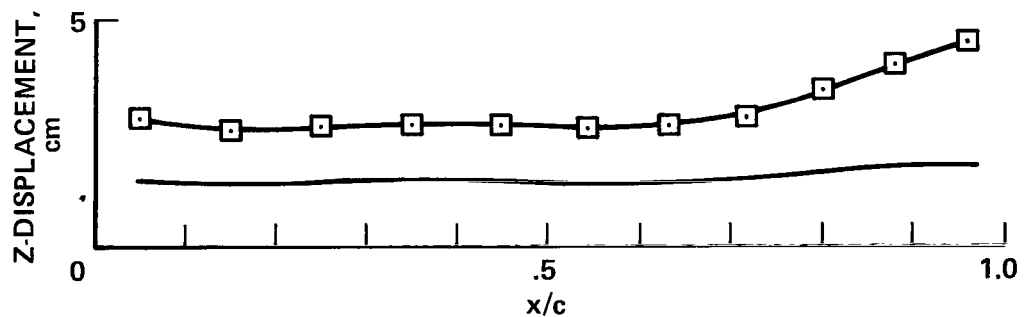


(b) 35.44% semispan.

Figure 13.- Orbiter wing deformation.

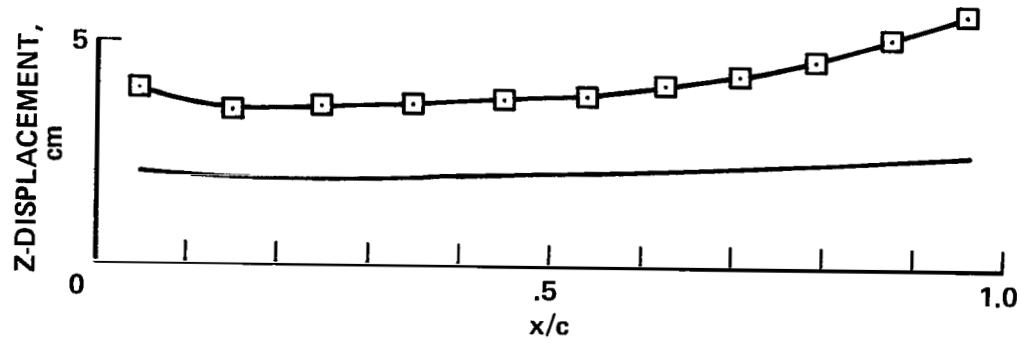


(c) 44.20% semispan.

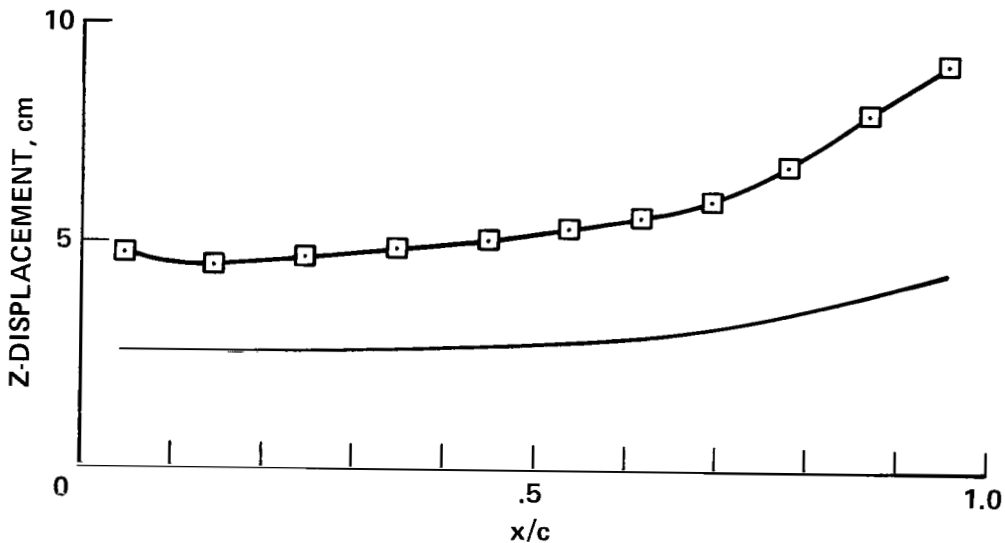


(d) 52.74% semispan.

Figure 13.- Continued.

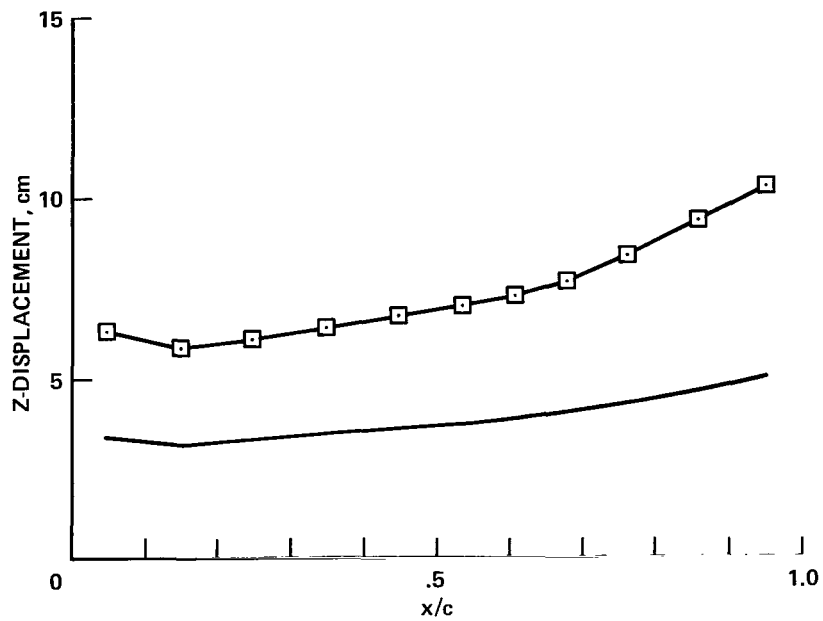


(e) 61.28% semispan.

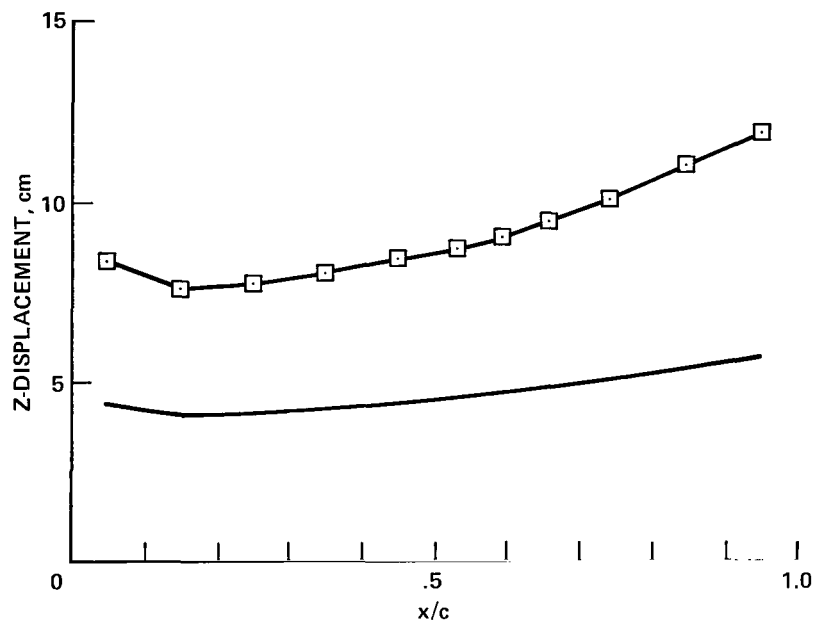


(f) 69.82% semispan.

Figure 13.- Continued.

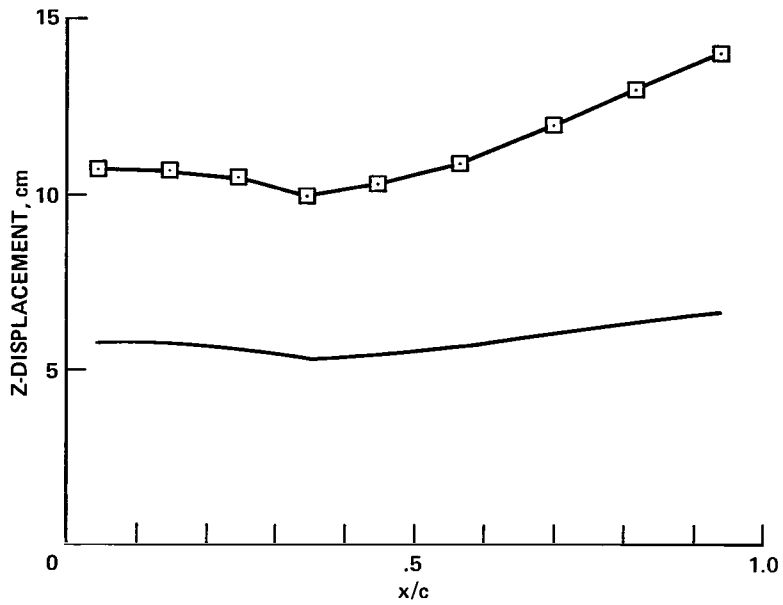


(g) 78.36% semispan.



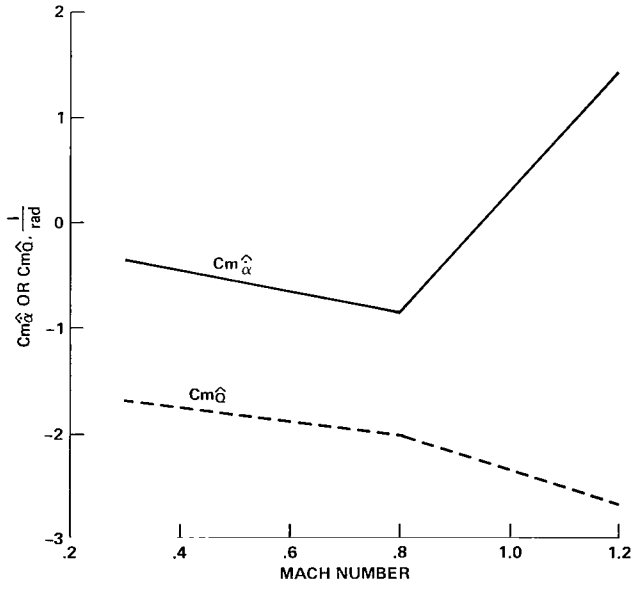
(h) 86.9% semispan.

Figure 13.- Continued.



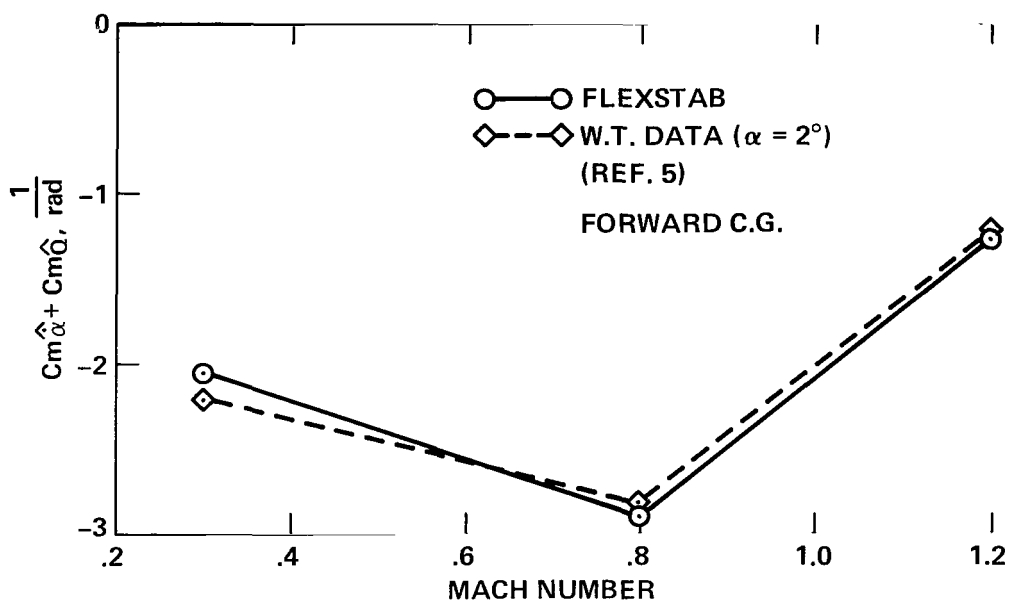
(i) 95.44% semispan.

Figure 13.- Concluded.



(a) Calculated  $C_{m\hat{\alpha}}$  and  $C_{m\hat{Q}}$ .

Figure 14.- Variation of  $C_{m\hat{\alpha}}$  and  $C_{m\hat{Q}}$  with Mach number.



(b) Calculated and experimental  $C_{m\hat{\alpha}} + C_{m\hat{Q}}$ .

Figure 14.- Concluded.

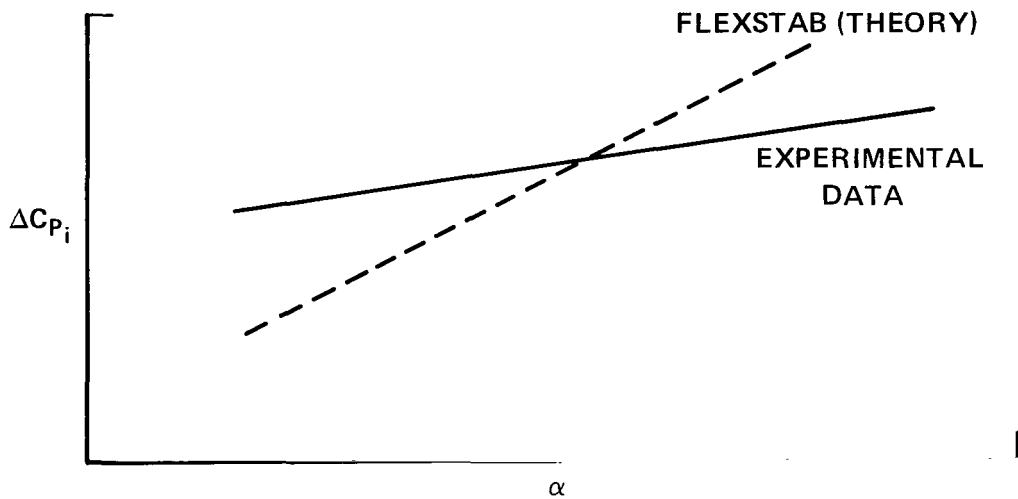


Figure 15.- Variation of  $\Delta C_{P_i}$  with angle of attack.

1. Report No. NASA TP-1179	2. Government Accession No.	3. Recipient's Catalog No.	
4. Title and Subtitle STATIC AND DYNAMIC STABILITY ANALYSIS OF THE SPACE SHUTTLE VEHICLE-ORBITER		5. Report Date March 1978	
7. Author(s) Wei J. Chyu, Ralph K. Cavin,* and Larry L. Erickson		6. Performing Organization Code	
9. Performing Organization Name and Address NASA Ames Research Center Moffett Field, Calif. 94035		8. Performing Organization Report No. A-7217	
12. Sponsoring Agency Name and Address National Aeronautics and Space Administration Washington, D.C. 20546		10. Work Unit No. 505-02-21-08-00	
15. Supplementary Notes  *Texas A&M University, College Station, Tex. 77843		11. Contract or Grant No.	
16. Abstract  The longitudinal static and dynamic stability of a Space Shuttle Vehicle-Orbiter (SSV Orbiter) model is analyzed using the FLEXSTAB computer program. Nonlinear effects are accounted for by application of a correction technique in the FLEXSTAB system; the technique incorporates experimental force and pressure data into the linear aerodynamic theory. A flexible Orbiter model is treated in the static stability analysis for the flight conditions of Mach number 0.9 for rectilinear flight (1 g) and for a pull-up maneuver (2.5 g) at an altitude of 15.24 km. Static stability parameters and structural deformations of the Orbiter are calculated at trim conditions. For the dynamic stability analysis, the characteristics of damping in pitch are investigated for a Mach number range of 0.3 to 1.2. The calculated results for both the static and dynamic stabilities are compared with the available experimental data. These comparisons show that it is necessary to use the correction technique due to the nonlinearity. The calculated results indicate that the elevon effectiveness and the longitudinal stability are lower for the elastic Orbiter model than for the rigid model. The g effect on the trim solutions is significant for both the rigid and flexible models. Calculated pitch damping is in good agreement with the experimental results.			
17. Key Words (Suggested by Author(s)) Space Shuttle Vehicle-Orbiter Aerodynamic stability Aeroelasticity		18. Distribution Statement Unlimited	
		STAR Category - 01	
19. Security Classif. (of this report) Unclassified	20. Security Classif. (of this page) Unclassified	21. No. of Pages 61	22. Price* \$4.50

\*For sale by the National Technical Information Service, Springfield, Virginia 22161

NASA-Langley, 1978

National Aeronautics and  
Space Administration

Washington, D.C.  
20546

Official Business  
Penalty for Private Use, \$300

THIRD-CLASS BULK RATE

Postage and Fees Paid  
National Aeronautics and  
Space Administration  
NASA-451



3 11U,A, 031378 S00903DS  
DEPT OF THE AIR FORCE  
AF WEAPONS LABORATORY  
ATTN: TECHNICAL LIBRARY (SUL)  
KIRTLAND AFB NM 87117

POSTMASTER: If Undeliverable (Section 158  
Postal Manual) Do Not Return

NASA

S